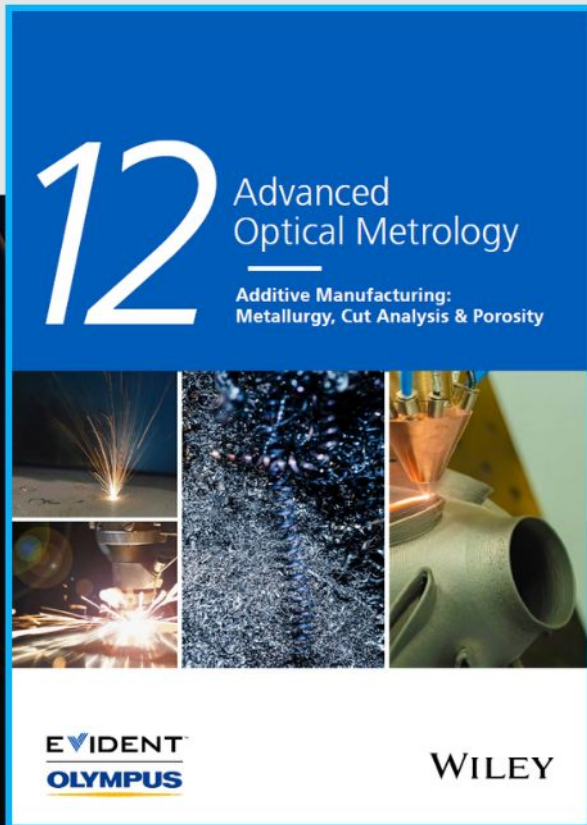




Additive Manufacturing: Metallurgy, Cut Analysis & Porosity



The latest eBook from
Advanced Optical Metrology.
Download for free.

In industry, sector after sector is moving away from conventional production methods to additive manufacturing, a technology that has been recommended for substantial research investment.

Download the latest eBook to read about the applications, trends, opportunities, and challenges around this process, and how it has been adapted to different industrial sectors.

EVIDENT™
OLYMPUS

WILEY

PillarX: A Microfluidic Device to Profile Circulating Tumor Cell Clusters Based on Geometry, Deformability, and Epithelial State

Brenda J. Green,* Margherita Marazzini, Ben Hershey, Amir Fardin, Qingsen Li, Zongjie Wang, Giovanni Giangreco, Federica Pisati, Stefano Marchesi, Andrea Disanza, Emanuela Frittoli, Emanuele Martini, Serena Magni, Galina V. Beznoussenko, Claudio Vernieri, Riccardo Lobefaro, Dario Parazzoli, Paolo Maiuri, Kristina Havas, Mahmoud Labib, Sara Sigismund, Pier Paolo Di Fiore, Rosalind H. Gunby, Shana O. Kelley, and Giorgio Scita*

Circulating tumor cell (CTC) clusters are associated with increased metastatic potential and worse patient prognosis, but are rare, difficult to count, and poorly characterized biophysically. The PillarX device described here is a bimodal microfluidic device (Pillar-device and an X-magnetic device) to profile single CTCs and clusters from whole blood based on their size, deformability, and epithelial marker expression. Larger, less deformable clusters and large single cells are captured in the Pillar-device and sorted according to pillar gap sizes. Smaller, deformable clusters and single cells are subsequently captured in the X-device and separated based on epithelial marker expression using functionalized magnetic nanoparticles. Clusters of established and primary breast cancer cells with variable degrees of cohesion driven by different cell-cell adhesion protein expression are profiled in the device. Cohesive clusters exhibit a lower deformability as they travel through the pillar array, relative to less cohesive clusters, and have greater collective invasive behavior. The ability of the PillarX device to capture clusters is validated in mouse models and patients of metastatic breast cancer. Thus, this device effectively enumerates and profiles CTC clusters based on their unique geometrical, physical, and biochemical properties, and could form the basis of a novel prognostic clinical tool.


1. Introduction

Metastasis begins with invasion of primary tumor cells into the surrounding tissues. Cells that successfully intravasate into the vasculature become CTCs that can exist either as single cells or as clusters.^[1–3] Cancer cells belonging to the same cluster can be highly heterogeneous, however they typically express epithelial cell–cell adhesion proteins.^[4]

CTC clusters are usually small (2–50 cells) and rare in circulation but they possess up to 50-fold increased metastatic potential compared to individual CTCs.^[3,5] Several groups have used different technologies to detect CTC clusters in patients with early and metastatic epithelial cancers.^[6–9] The continuous presence of elevated counts of CTC clusters in the blood of patients with metastatic breast and prostate cancer is shown to correlate with poor prognosis and shorter

B. J. Green, M. Marazzini, B. Hershey, Q. Li, F. Pisati, S. Marchesi, A. Disanza, E. Frittoli, E. Martini, S. Magni, G. V. Beznoussenko, C. Vernieri, R. Lobefaro, D. Parazzoli, P. Maiuri, K. Havas, G. Scita
IFOM-FIRC Institute of Molecular Oncology
Via Adamello, 16, Milan 20139, Italy
E-mail: brenda.green@ifom.eu; giorgio.scita@ifom.eu

A. Fardin, G. Giangreco, S. Sigismund, P. P. D. Fiore, R. H. Gunby
IEO
Istituto Europeo di Oncologia IRCCS
Via Ripamonti 435, Milan 20141, Italy

 The ORCID identification number(s) for the author(s) of this article can be found under <https://doi.org/10.1002/smll.202106097>.

© 2022 The Authors. Small published by Wiley-VCH GmbH. This is an open access article under the terms of the Creative Commons Attribution License, which permits use, distribution and reproduction in any medium, provided the original work is properly cited.

DOI: [10.1002/smll.202106097](https://doi.org/10.1002/smll.202106097)

Z. Wang, S. O. Kelley
Institute for Biomaterials and Biomedical Engineering
University of Toronto
144 College St, Toronto, Ontario M5S 3M2, Canada

G. Giangreco
Tumour Cell Biology Laboratory
The Francis Crick Institute
1 Midland Rd, London NW1 1AT, UK

C. Vernieri, R. Lobefaro
Fondazione IRCCS Istituto Nazionale dei Tumori
Via G. Venezian 1, Milan 20133, Italy

S. Sigismund, P. P. D. Fiore, G. Scita
Department of Oncology and Haemato-Oncology
Università degli Studi di Milano
Via Festa del Perdono, 7, Milan 20122, Italy

M. Labib, S. O. Kelley
Department of Chemistry
Northwestern University
2145 Sheridan Road, Evanston, IL 60208, USA

progression-free survival, relative to patients with fewer circulating clusters.^[3,10] In the hostile environment of the blood vessels, clustering of cancer cells may protect against fluid shear stress, oxidative stress, or immune attack.^[11–13] Clustering facilitates multiclonal interactions between cells displaying different epithelial-to-mesenchymal transition (EMT) states, ultimately increasing their potential for colonization at biologically and mechanically diverse distant sites.^[12,14,15]

Mechanical adaptability of tumor cells to various environmental conditions has been linked to metastatic potential.^[2,16–25] In particular, cancer cells isolated from breast, lung, or pancreatic cancer patients were shown to be 80% softer compared to non-malignant cells.^[26] Consistently, tumor cells surviving shear stress in the circulation show reduced F-actin assembly and stiffness relative to untreated cells.^[11] This might enable CTC cells to more efficiently dissipate force and withstand mechanical stress. Clustering of cancer cells has been further implicated in mechanical protection against hostile hemodynamic forces.^[2] Thus, there is an emerging interest in developing diagnostic devices that are capable of capturing, sorting and recovering individual CTCs and clusters based on their mechanical properties.

Several methods have been developed for CTC capture from blood, including antigen-dependent and -independent techniques or a combination of both.^[27–29] Antigen-dependent approaches include antibody-functionalized microfluidic structures,^[30–32] the application of nucleic acid aptamers to target rare cells^[33] and hydrodynamic sorting devices.^[34] Antigen-independent approaches comprise porous filtration devices,^[35–38] the size-restriction Parsortix device,^[3,39] inertial microfluidics^[40,41] and deterministic lateral displacement techniques.^[42]

Alternatively, CTC deformation devices use conical-shaped microfilters, micro-pillars, and vortex-mediated deformability cytometry which traps individual cancer cells based on their difference in stiffness or separates them relative to white blood cells (WBCs).^[43–49] However, there is not yet a system that can simultaneously sort malignant cell clusters according to multiple physical parameters, such as deformability, size, and cellular properties.

Here, we employed a microfluidic strategy, using a Pillar-device and X-device connected in series (PillarX) which efficiently captures and sorts CTC clusters from whole blood. Microfluidic pillar structures have been previously used to separate CTC clusters from blood samples.^[42] The X-device is a technology that we designed and validated for sorting CTCs from whole blood using magnetic nanoparticles (MNPs).^[50–52] While these two devices alone are not novel, when we connect them in series, they provide a unique ability to sort clusters based on size, epithelial expression, and deformability. This multi-factor sorting is not possible if the chips are run separately, and provides our system with significant advantages over existing CTC devices. With this device, we present a simplified tool for the determination of cluster size, composition (including WBC contribution) and relative cohesive properties, which are otherwise difficult to determine.

1.1. Design of the PillarX Device

The system is composed of two devices connected in series, the Pillar-device and the X-device (Figure 1a). Cells in whole

blood are initially labelled with epithelial cell adhesion molecule (EpCAM) antibodies conjugated to MNPs. EpCAM is nearly exclusively expressed on epithelial cells and is used as a marker of circulating carcinoma cells that retain an epithelial identity.^[53,54] Pre-labelled cells are then loaded, at a constant flow rate of 750 $\mu\text{L h}^{-1}$, into the Pillar-device, which separates single cells and clusters based on size and deformability. The Pillar-device is composed of six zones (P1–P6) of 100 μm -tall polydimethylsiloxane (PDMS) micro-pillars separated by progressively smaller gaps that sort clusters and single cells ranging from 20 to 200 μm in diameter (Table S1 and Figure S1a,b, Supporting Information). Large and rigid clusters are trapped in earlier zones, while small clusters and large single cells are trapped in the last zone (Figure 1b,c). The pillar gaps are also designed to maximize the capture of CTC clusters, which have diameters $> 20 \mu\text{m}$,^[5] and minimize the capture of non-specific WBCs, which have diameters of 7–14 μm (Figure S2, Supporting Information).^[55] The symmetrical pillar shape also allows for efficient release of cells.^[45]

More deformable clusters, along with the majority of single cells, flow into the X-device where they are separated based on epithelial expression using EpCAM-conjugated MNPs (Figure 1a). An external array of magnets placed under the X-device enables the high-efficiency capture of MNP-labelled cells in the low-flow regions around the grooves of the X-structures. Cells and clusters with high EpCAM will have a greater number of EpCAM-MNPs and experience a higher magnetic force and are captured in early zones, whereas cells and clusters with fewer EpCAM-MNPs experience a lower magnetic force and are captured in later zones. The X-device contains X-shaped PDMS micro-structures that increase in height in a stepwise manner from 50 to 400 μm across 8 zones (X1–X8; Table S2 and Figure S1c,d, Supporting Information). This increase in cross-section area leads to a reduction in linear velocity in each zone, which increases the probability of capturing low-EpCAM expressing cells in later zones^[51,52,56] (Figure 1b,c; Microfluidic Set up: Figure S3, Supporting Information).

Cells can be released from the PillarX device and further analyzed. Release from the Pillar-device is achieved by the application of a high flow rate (5000 $\mu\text{L h}^{-1}$) in reverse flow, while for the X-device, a forward flow (5000 $\mu\text{L h}^{-1}$) in the absence of the magnetic field is used. Together, the PillarX device enables the sorting of single cells and clusters based on size, deformability, and epithelial marker expression levels.

1.2. Modeling of Velocity, Shear Stress, and Pressure in the PillarX Device

We used Comsol software to model fluid flow in the PillarX device considering both capture and release conditions. These models estimated capture velocity profiles around the Pillars and X-structures ranging from 79 to 664 $\mu\text{m s}^{-1}$ (Figure 2a,b). These flow conditions were associated with minimal shear stress ($< 0.20 \text{ Pa}$) acting on the cells during capture, which is well-below the maximum physiological range of 1–3 Pa^[57] (Figure 2c,d). As previously reported, shear stress $> 2 \text{ Pa}$ results in disaggregation of clusters;^[57] thus our system favors gentle capture conditions for clusters considering low shear stress and low applied

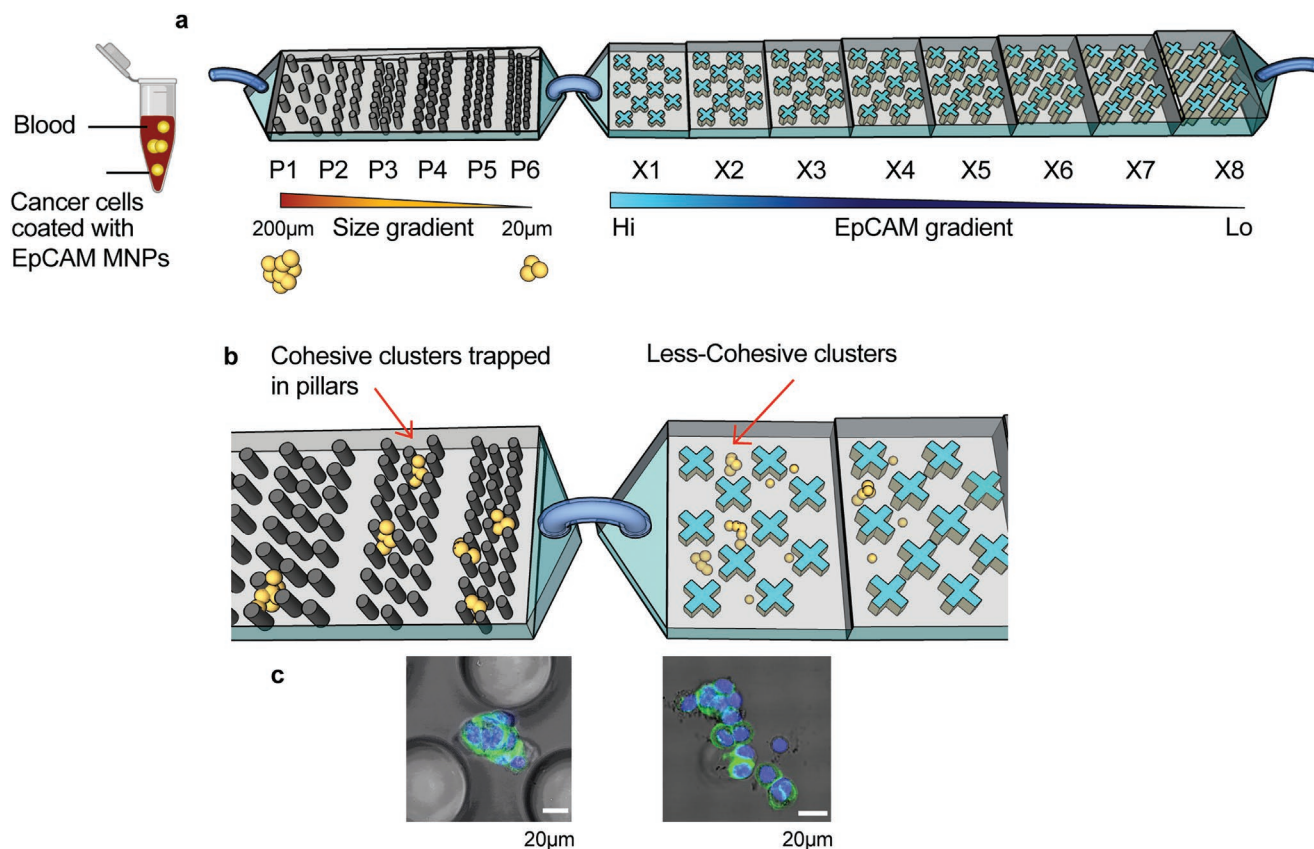


Figure 1. Overview of the PillarX device design. a) Microfluidic device design for capture of CTCs and CTC clusters in whole blood are initially labelled with EpCAM specific antibodies conjugated to magnetic nanoparticles. Labeled cells are introduced into the microfluidic device at a flow rate of $750 \mu\text{L h}^{-1}$. Large and more rigid cohesive clusters are trapped in the Pillar-device consisting of 6 zones (P1–P6), with decreasing pillar gap sizes ranging from 200 to 20 μm . More deformable clusters and single cells pass into the X-device, consisting of 8 zones (X1–X8) containing X-shaped microstructures ranging from 50 to 400 μm in height, which separate cells based on EpCAM expression using the magnetic nanoparticles. b) Zoomed-in window of P4–P6 of the Pillar-device and X1–X2 of the X-device. c) Representative immuno-staining images of MCF10DCIS clusters trapped in P5 of the Pillar-device (left) and X1 of the X-device (right). Cells were immuno-stained with AF488-labeled anti-E-cadherin (green) and DAPI (blue).

pressures. Details of shear stress simulations, velocity and pressure within the microfluidic devices are outlined in the Supporting Information (Figure S4, Supporting Information, and Experimental Section “Device design and fluid modeling”).

For the release flow modeling, we obtained velocity, shear stress, and pressure profiles, which although higher than the capture conditions (maximum shear stress of 1.3 Pa and applied pressure of 498 Pa), were still indicative of gentle release conditions (Figure 2c,d). Indeed, existing constriction and shear flow-based deformability devices, which are mainly used for single cell analysis, have applied pressures of ≈ 1 kPa, and have been shown to deform cells along the channel walls or within a fluid environment.^[58–60]

1.3. Characterization of Cell Models Used for PillarX Device Validation

Breast cancer cells generate clusters in vitro and in vivo and have been extensively used for the validation of CTC devices.^[3,39] We used the human breast cancer cell lines, MCF10DCIS and MDA-MB-231, as models of in vivo CTCs, to validate the PillarX device.

These cell lines display different degrees of aggressiveness, and levels of EMT with variable expression of mesenchymal versus epithelial genes, especially those involved in cell–cell adhesion.^[12,61–63] Genes such as E-cadherin (*CDH1*), plakoglobin (*JUP*), N-cadherin (*CDH2*), EpCAM (*EPCAM*), and claudin-3 (*CLDN3*) are key determinants of cell–cell junctions, influencing their structure, strength, and response to tensile stress.^[64,65] Thus, they are also expected to have a major impact on cluster cohesion,^[66] which in turn, has been implicated in mechanical adaptability both in circulation and during invasion.^[16–25] We tested this theory directly by increasing cell adhesion through the expression of E-cadherin in MDA-MB-231 cells or by selecting a more mesenchymal isogenic population of MCF10DCIS cells.

1.4. Cluster Cohesion Is Influenced by the Expression of E-Cadherin in MDA-MB-231 Cells and by the Mesenchymal State of Malignant MCF10DCIS Cells

MDA-MB-231 is a model of highly metastatic mesenchymal breast cancer cells which leads to invasive metastatic carcinoma in vivo: the cells display elevated *ZEB1* (Cycle threshold,

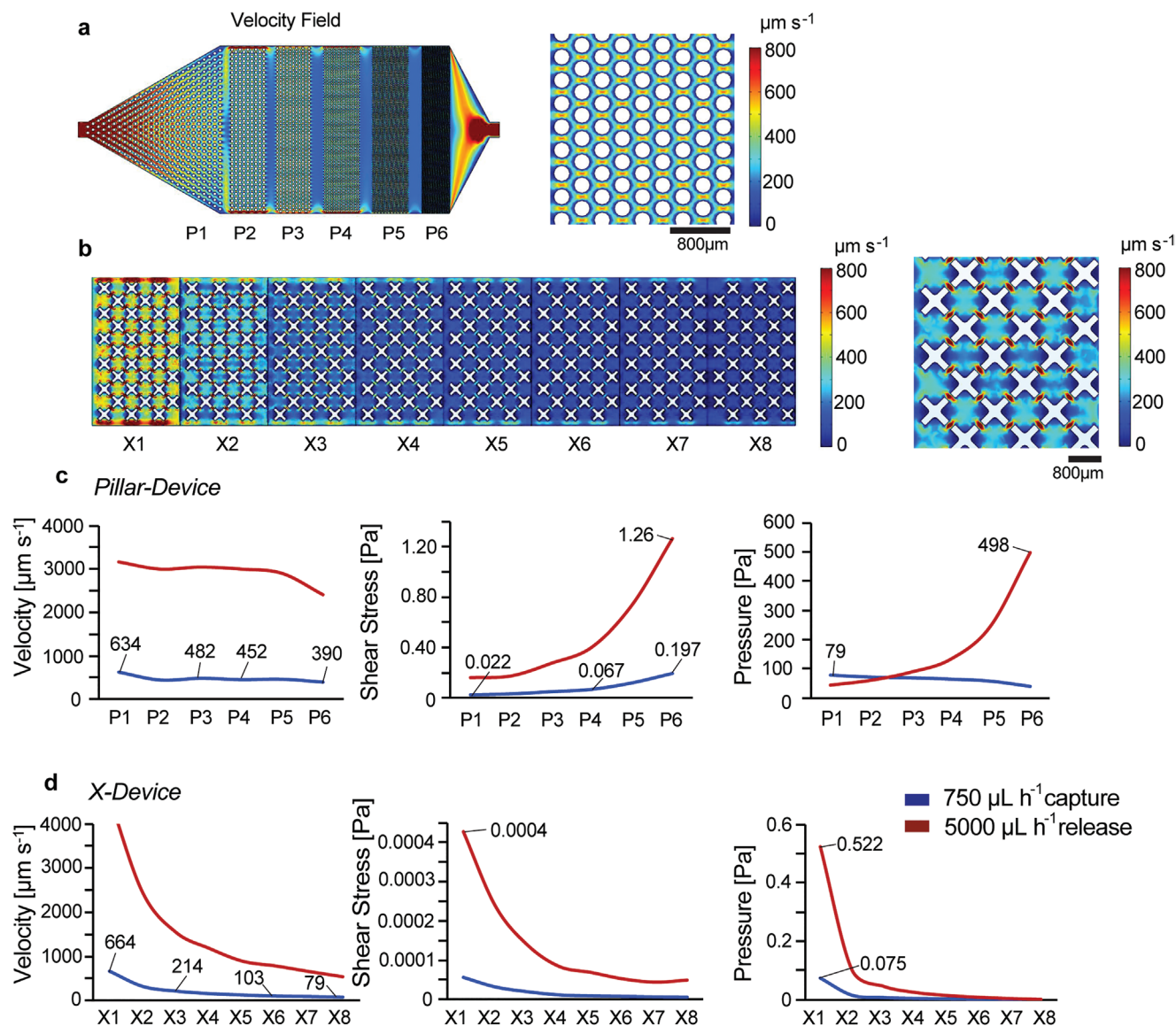
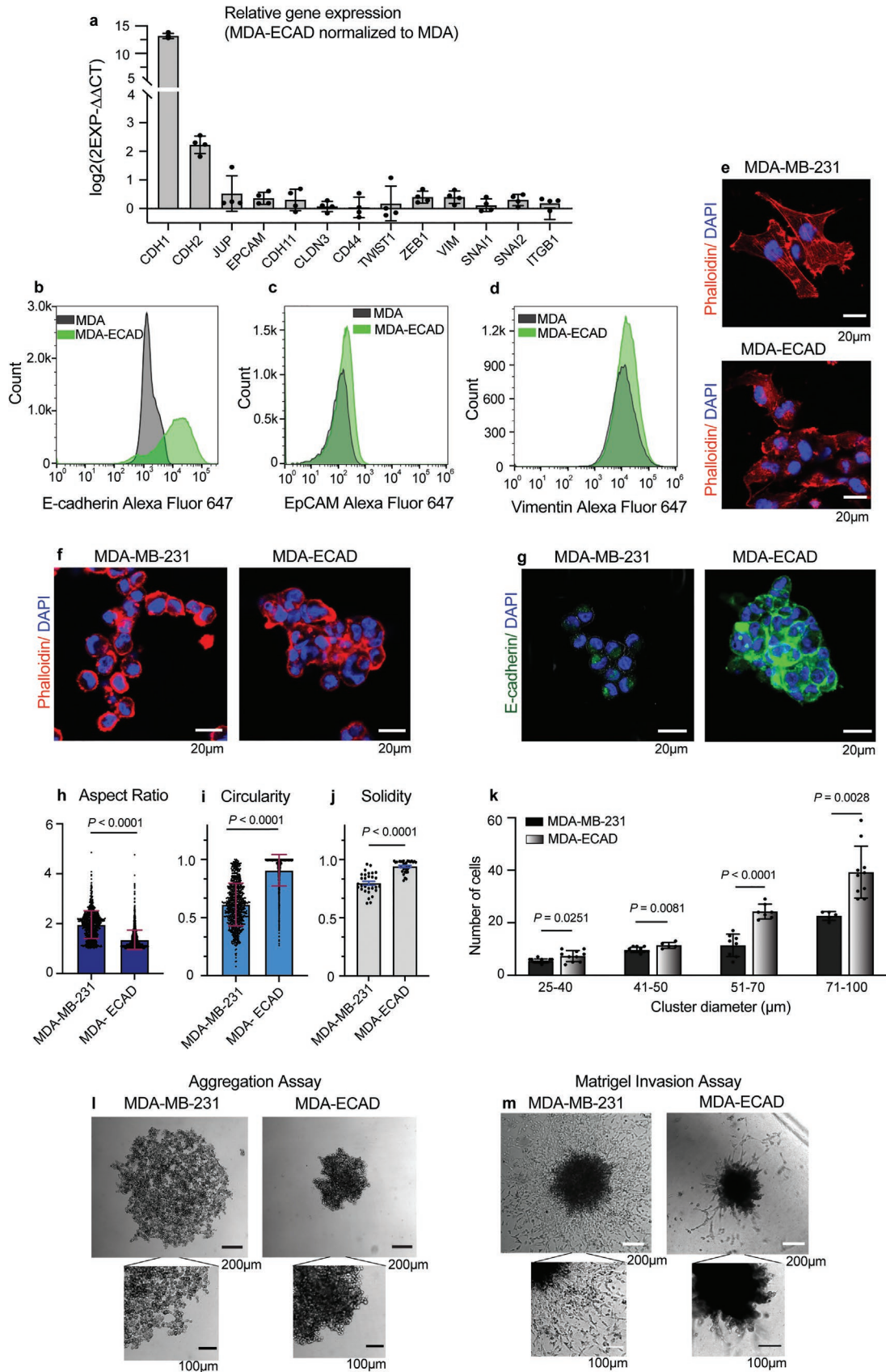


Figure 2. Comsol modeling of the Pillar-device and the X-device. a) Velocity field for capture through the Pillar-device. The right image illustrates a zoomed-in window of P2. b) Velocity field for capture through the X-device. The right image illustrates a zoomed-in window of X2. c,d) Velocity, shear stress, and applied pressures profiles for the Pillar- and X-device. Fluid modeling was considered for both capture ($750 \mu\text{L h}^{-1}$) and release ($5000 \mu\text{L h}^{-1}$) conditions.

Ct = 25), *SNAI2* (Ct = 26), and *VIM* levels (Ct = 19) and low expression of the epithelial cell–cell adhesion marker *CDH1* (E-cadherin; Ct = 33).^[67,68] Among the multiple players involved in the regulation of cell–cell adhesion, E-cadherin plays an overarching role in mediating cell adhesion strength and junction reinforcement when subjected to tensile stress.^[69] In cancer progression, E-cadherin has been implicated in both tumor suppression and promotion.^[70–72] To examine how this protein influences cell–cell adhesion within clusters, we expressed GFP-tagged murine E-cadherin in MDA-MB-231 cells (MDA-ECAD) (Figure S5a, Supporting Information). MDA-ECAD cells maintained low levels of epithelial and cell–cell adhesion proteins, such as *EPCAM* and *CLND3* (Ct = 29 and 30, respectively), alongside high levels of *VIM* (Ct = 19) and *SNAI2* (Ct = 26), similar to the parental MDA-MB-231 cells (Figure 3a–d).

However, E-cadherin expression was sufficient to transform the mesenchymal spindle shape typical of MDA-MB-231 cells into a more epithelial-like cobblestone morphology on adhered surfaces (Figure 3e).

To measure cluster cohesiveness, we grew cells under low attachment conditions and analyzed clusters ranging in size from 5–40 cells. MDA-MB-231 formed loose, poorly adherent clusters, while MDA-ECAD generated more compact clusters (Figure 3f,g). MDA-ECAD clusters also exhibited significantly lower aspect ratios, higher circularity and solidity (i.e., solidity = area/convex area, this is a proxy of the cluster density while taking into account the contour), and increased cluster cell density (i.e., number cells/area) compared to MDA-MB-231 clusters, indicating that E-cadherin expression influences cluster shape and cohesiveness (Figure 3h–k). We additionally



performed a time-lapse aggregation assay using a variable number of single cells (50 and 5000) and confirmed increased compactness of MDA-ECAD clusters relative to MDA-MB-231 clusters (Figure 3l; Figure S5b,c, Supporting Information). Addition of EGTA to the aggregation media interfered with tight cluster formation, suggesting that Ca²⁺-mediated cell–cell adhesions, such as those dependent on E-cadherin, are important for maintaining cohesiveness (Figure S5d, Supporting Information).

To relate the cell adhesive and cohesive properties to a relevant proxy of malignant progression, we employed 3D Matrigel invasion assays. We found that MDA-MB-231 clusters were more invasive and migrated as single cells, while MDA-ECAD were less invasive and exhibited a more prominent collective invasion (Figure 3m).

Next, we investigated the impact on cell cohesion of the transition toward a plastic mesenchymal state in MCF10DCIS cells. Plasticity in EMT has been shown to drive tumor progression and invasion, and directly influences cell–cell adhesion strength and, possibly, cohesion.^[63] MCF10DCIS cells express oncogenic T24-H-RAS and are models of early-stage breast ductal carcinoma in situ (DCIS) that can progress to invasive carcinoma when injected into immuno-compromised mice.^[73] They display an intermediate EMT state, with the concomitant expression of a number of epithelial markers, such *CDH1*, *JUP*, and *EPCAM* (Ct = 24, 24, and 25, respectively), low levels of key EMT transcription factors, but elevated expression of mesenchymal proteins, such as *VIM* (Ct = 21) and *ITGB1* (Ct = 23).^[73–75] We exploited the intermediate and reversible state of these cells to isolate an isogenic cell population via *Twist1* over-expression in MCF10DCIS cells, followed by FACS sorting for low *Epcam*. These cells displayed a mixed but more mesenchymal set of traits (MCF10DCIS-Mes).

MCF10DCIS-Mes cells had reduced mRNA expression of epithelial markers, *CDH1*, *EPCAM*, and *JUP*, and increased levels of mesenchymal markers, *CDH2*, *CDH11*, and *ZEB1*, compared with parental MCF10DCIS cells. However, these cells also showed reduced expression of the mesenchymal genes *VIM*, *SNAI2*, and *ITGB1*, in keeping with their partial EMT identity (Figure 4a). The plasticity of this partial EMT state was revealed by flow cytometry analysis, which showed that, despite the initial selection of a homogeneous cell population, MCF10DCIS-Mes cells gave rise upon culturing to a mixed epithelial and mesenchymal cell population (Figure 4b–d; Figure S6a,

Supporting Information). The acquisition of mesenchymal markers in MCF10DCIS-Mes cells was mirrored by the loss of polygonal shapes and the formation of F-actin-rich, prominent lamellipodia-like protrusions (Figure 4e).

Measurement of cluster cohesion using cells grown under low attachment conditions indicated that MCF10DCIS-Mes clusters were less spherical, had more irregular contours (higher aspect ratio, reduced circularity and solidity) (Figure 4f–j), but displayed similar cell densities relative to parental MCF10DCIS clusters (Figure 4k). These observations suggest that the partial EMT state of MCF10DCIS-Mes cells is associated with reduced cluster cohesiveness; albeit observed by the overall cluster shape rather than the cell density. Consistently, in an aggregation assay, MCF10DCIS-Mes cells formed relatively compact but less spherical clusters that display an irregular contour, consistent with their reduced solidity (Figure 4l; Figure S6b,c, Supporting Information). Furthermore, addition of EGTA interfered with MCF10DCIS cluster formation showing dependency on Ca²⁺-mediated cell–cell adhesions, as observed also for MDA-ECAD cells (Figure S6d, Supporting Information).

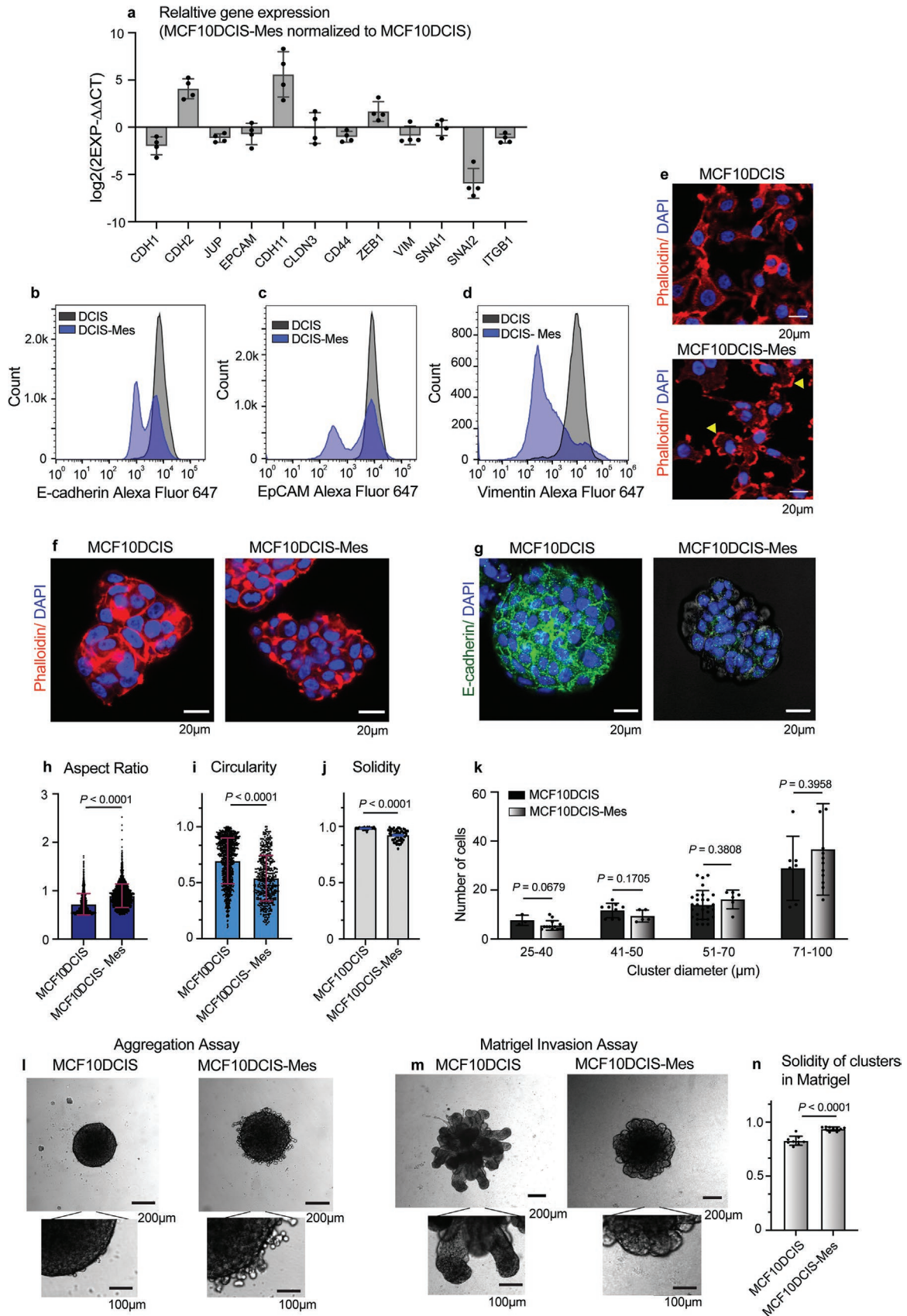
In 3D Matrigel invasion assays, MCF10DCIS-Mes clusters showed a reduction in collective invading buds in Matrigel, compared with parental cells, in line with the reduced cohesiveness of these cells (Figure 4m). This change in invading cluster contour was quantitatively measured by the increased solidity of MCF10DCIS-Mes clusters in Matrigel relative to the parental line (Figure 4n).

Together, these data show that increased E-cadherin levels in MDA-MB-231 cells results in increased cluster cohesion and collective motility in Matrigel, while the selection of MCF10DCIS cells with increased mesenchymal traits results in reduced cell cohesion and collective motility behavior. We therefore used these diverse cell lines to validate the PillarX device, as models of breast cancer CTC clusters with varying levels of cell–cell adhesion proteins.

1.5. The PillarX Device Profiles Clusters Based on Their Size, Cohesiveness and Epithelial Identity

We designed the PillarX device to efficiently capture both single cells and clusters and sort them based on their size, cohesiveness, and epithelial identity. To verify these design principles,

Figure 3. The expression of E-cadherin in MDA-MB-231 cells increases cluster cohesiveness. a) qRT-PCR analysis of EMT and cell–cell adhesion gene expression. $\Delta Ct = Ct_{\text{gene}} - Ct_{\text{gapdh}}$. $\Delta\Delta Ct = \Delta Ct_{\text{MDA-ECAD}} - \Delta Ct_{\text{MDA}}$. *CDH1* (E-cadherin), *CDH2* (N-cadherin), *JUP* (plakoglobin), *EPCAM* (epithelial cell adhesion molecule), *CDH11* (cadherin-11 surface glycoprotein), *CLDN3* (Claudin-3 tight junction protein), *CD44* (cell-adhesion protein), *TWIST1*, *ZEB1*, *SNAI1* and *SNAI2* (EMT transcription factors), *VIM* (vimentin), *ITGB1* (integrin $\beta 1$). Data are mean \pm s.d. of biological replicates ($n = 4$). Dots represent experimental repeats. b–d) Analysis of E-cadherin, *Epcam*, and Vimentin protein expression by flow cytometry. Cells were labeled with anti-E-cadherin, anti-*Epcam*, or anti-Vimentin conjugated to Alexa Fluor 647. e) Morphological analysis of MDA-MB-231 and MDA-ECAD cells in adherence conditions by immuno-staining with phalloidin-TRITC and DAPI. f,g) Representative images of MDA-MB-231 and MDA-ECAD clusters generated in low attachment cultures. Clusters were labeled with phalloidin-TRITC/DAPI and anti-E-cadherin conjugated to Alexa Fluor 488/DAPI, respectively. h–j) Aspect ratio, circularity, and solidity of MDA-MB-231 and MDA-ECAD clusters measured from clusters grown under low attachment conditions. Measurements were obtained using ImageJ analyze particles program. k) Quantification of cluster cell density from DAPI stained clusters generated under low attachment conditions. Data are plotted as the number of cells per clusters of different areas: $n = 38$ for MDA-MB-231 clusters and 32 for MDA-ECAD clusters, from 3 independent experiments. h–k) Data are mean \pm s.d. of 3 independent repeats. p -values were calculated using an unpaired two-tailed Student's t -test. Dots represent individual clusters. l) Aggregation assay. MDA-MB-231 and MDA-ECAD cells were grown in 96-well plates (5000 cells/well) under low attachment conditions and aggregation was assessed after 24 h of culture. m) Matrigel invasion assay. Cells grown as in (l) for 24 h were transferred to 5 mg mL⁻¹ Matrigel in media and invasion was assessed at 48 h. Magnifications are shown below (l,m).



we used the above-described cell lines as models of breast cancer CTC clusters with varying levels of cell–cell adhesion proteins, cell cohesiveness, and epithelial state.

To prepare samples for loading in the PillarX device, we focused on analyzing small clusters (2–50 cells) to mimic in vivo CTC sizes. Cells were cultured under low attachment to generate clusters and subsequently filtered to remove larger clumps. Next, clusters and cells were fluorescently labelled and spiked into a mixture of blood obtained from NOD scid gamma (NSG) mice and anti-EpCAM MNPs, prior to introduction in the microfluidic device at a low flow rate of $750 \mu\text{L h}^{-1}$ (Figure 5a). Verification of EpCAM-MNPs binding to cells are shown in Figure S7, Supporting Information, where we observe a greater number of beads binding to MCF10DCIS cells relative to MDA-MB-231 cells. Importantly, we also confirmed that EpCAM-MNPs do not induce artificial aggregation of cells in suspension (Figures S8, Supporting Information). This mixture of single cells and clusters in a blood cell background was created to mimic in vivo CTCs, while the flow rate was chosen to preserve cluster integrity. To quantify the cells/clusters captured in the different zones of the device, we developed a semi-automated counting method based on the ImageJ particles algorithm (Figure S9, Supporting Information, and Experimental Section “Semi-automated counting procedure”). This method uses an empirically derived coefficient to estimate the number of cells in a given cluster of defined area. The capture efficiency is then determined by comparing the number of captured cells/clusters with respect to the total cells loaded into the device. The PillarX device efficiently and specifically trapped breast cancer clusters and cells, with mean capture efficiencies ranging from 75–84% (Figure 5b). Notably, the non-specific capture of MDA-MB-231 and MCF10DCIS single cells (with diameters $< 20 \mu\text{m}$) was less than 1% in the Pillar-device (Figure S10a, Supporting Information). Similarly, capture of NIH-3T3 fibroblasts expressing low levels of EpCAM in the X-device was below 10% (Figure S10b, Supporting Information).

Comparative analysis of the profiles of MDA-MB-231 versus MDA-ECAD cells revealed distinct capture distributions that depended on cluster size, cohesiveness, and epithelial cell identity. MDA-MB-231 cells formed smaller clusters on average, compared with MDA-ECAD (Figure 5c), and this was reflected in the Pillar-device profiles. MDA-MB-231 clusters were captured in P6, while MDA-ECAD clusters were captured in P3–P6

(Figure 5d). The distribution profiles in the X-device revealed that both MDA-MB-231 and MDA-ECAD cells/clusters were captured in the low-EpCAM zones. However, the MDA-ECAD profile shifted slightly to the left (with most of the cells found between zones X4–X7) with respect to the distribution of MDA-MB-231, which were primarily trapped between zones X5–X8. This shift is consistent with the slightly increased expression of EpCAM in MDA-ECAD relative to MDA-MB-231 cells (Figure 3c), demonstrating the sensitivity of the device to detect changes in cluster epithelial identity.

Size analysis of captured clusters indicated that the cluster diameters corresponded approximately to the gap dimension between pillars where they were trapped (Figure 5e). In some cases, however, the captured clusters had diameters smaller than the pillar gap dimension likely due to an irregular or elongated shape which caused them to orient across the gap. Clusters with diameters that exceeded the largest gap dimension were often trapped in the initial pillar row. Of note, we found that clusters in the X-device had mean diameters that were relatively equal across zones, and ranged from 24–38 μm . This observation indicates that breast cancer clusters can deform or topologically re-arrange to travel through the 20- μm gaps in P6. We observed a proportion of large ($>75 \mu\text{m}$ diameter) MDA-MB-231 clusters in the X-device; these clusters likely maintain weak adhesion as they re-arrange their shape to travel through the pillars; and re-form into an aggregate in the X-device.

Global, comparative analysis of cluster distribution of MDA-MB-231 and MDA-ECAD indicated that 61% of MDA-ECAD clusters were found between pillars. In contrast, the majority of less cohesive MDA-MB-231 clusters managed to navigate through P6 gaps and were captured in the X-device (Figure 5f). The increased probability of MDA-ECAD clusters to be captured between pillars with respect to MDA-MB-231 likely depends on their increased cluster size and cohesiveness.

Finally, on-chip immuno-staining revealed that MDA-MB-231 and MDA-ECAD clusters in the X-device had significantly lower E-cadherin levels compared with clusters trapped in the Pillar-device (Figure 5g,h), which correlates with their reduced cohesiveness and increased ability to pass through the micro-pillars.

Next, we compared the PillarX profiles of MCF10DCIS versus MCF10DCIS-Mes cells/clusters. MCF10DCIS cells formed larger clusters on average, compared to MCF10DCIS-Mes clusters, but both were efficiently captured in the PillarX device

Figure 4. Selection of a mesenchymal subpopulation of MCF10DCIS with altered cluster cohesiveness. a) qRT-PCR analysis of EMT and cell–cell adhesion gene expression. $\Delta\text{CT} = \text{CT}_{\text{gene}} - \text{CT}_{\text{gapdh}}$. $\Delta\Delta\text{CT} = \Delta\text{CT}_{\text{MCF10DCIS-Mes}} - \Delta\text{CT}_{\text{MCF10DCIS}}$. Data are mean \pm s.d. of biological replicates ($n = 4$). Dots represent experimental repeats. b–d) Analysis of E-cadherin, EpCAM, and Vimentin protein expression by flow cytometry. Cells were labeled with anti-E-cadherin, anti-EpCAM, or anti-Vimentin conjugated to Alexa Fluor 647. e) Morphological analysis of MCF10DCIS and MCF10DCIS-Mes cells plated on culture dish by immuno-staining with phalloidin-TRITC and DAPI. Yellow arrow heads indicate F-actin rich protrusions. f,g) Representative images of MCF10DCIS and MCF10DCIS-Mes clusters generated under low attachment cultures. Clusters were co-stained with phalloidin-FITC/DAPI, or with Alexa Fluor 488-conjugated anti-E-cadherin antibody/DAPI, respectively. h–j) Aspect ratio, circularity, and solidity of MCF10DCIS and MCF10DCIS-Mes clusters grown under low attachment conditions. Measurements were obtained using ImageJ analyze particles program. k) Quantification of cluster cell density from DAPI stained clusters generated under low attachment conditions. Data are plotted as the number of cells per clusters of different areas: $n = 47$ for MCF10DCIS clusters and 33 for MCF10DCIS-Mes clusters, from 3 independent experiments. l) Aggregation assay. MCF10DCIS and MCF10DCIS-Mes cells were grown in 96-well plates (5000 cells/well) under low attachment conditions and aggregation was assessed at 24 h. m) Matrigel invasion assay. Cells grown as in (l) for 24 h were transferred to 5 mg mL^{-1} Matrigel in media and invasion was assessed at 48 h. Magnifications are shown below (l,m). n) Solidity of MCF10DCIS and MCF10DCIS-Mes clusters in Matrigel quantified using the ImageJ analyze particles program. (h–k,n) Data are mean \pm s.d for 3 independent repeats. *p*-values were calculated using an unpaired two-tailed Student’s *t*-test. Dots represent individual clusters.

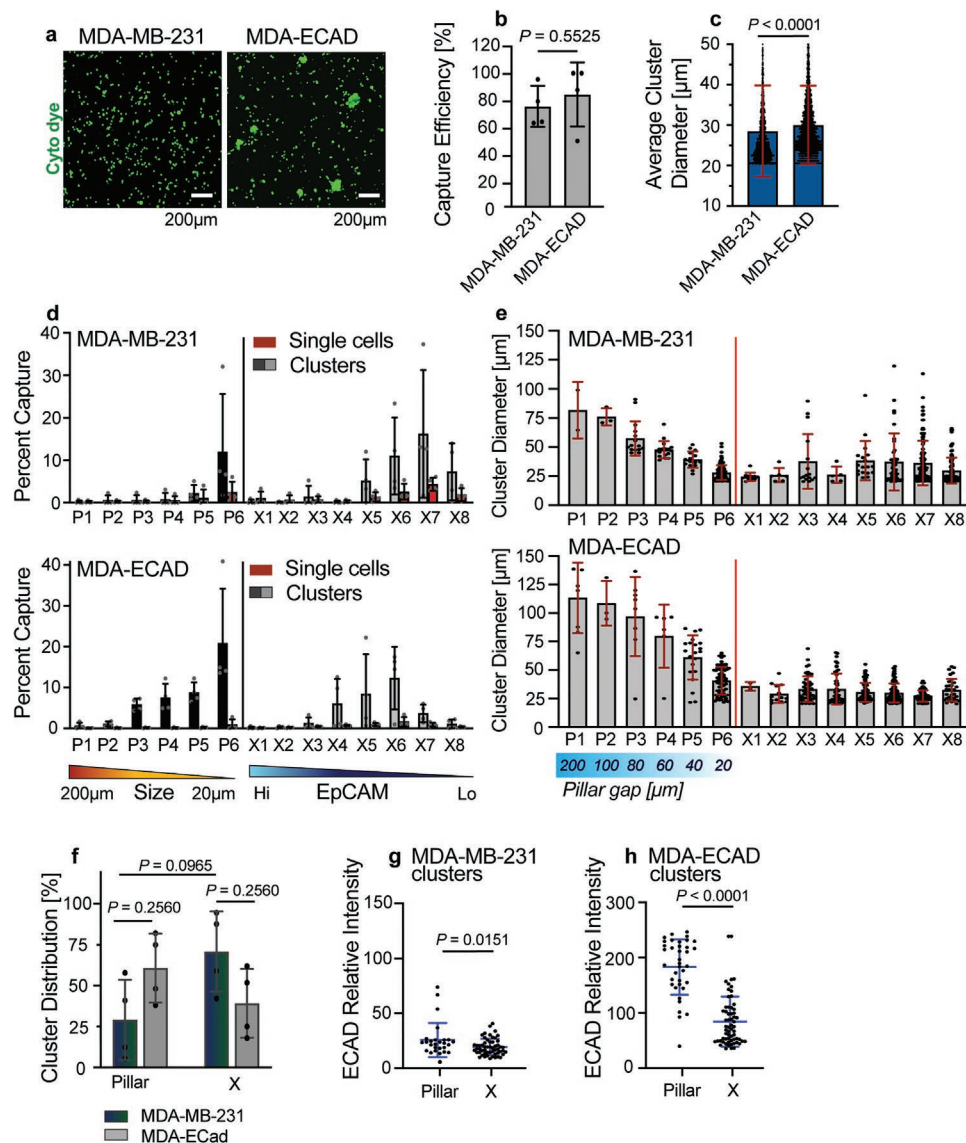


Figure 5. Expression of E-cadherin in MDA-MB-231 cells influences cluster cohesiveness and PillarX profiling. MDA-MB-231 and MDA-ECAD cells were cultured in low attachment conditions for 48 h, then mixed with 100 μL murine whole blood and anti-EpCAM MNPs, before loading into the PillarX device for profiling at $750 \mu\text{L h}^{-1}$ (4000 cells/clusters per sample). a) Representative images of cells and clusters generated in low attachment culture conditions. Cells were labeled with a green live cell cytoplasmic (cyto) tracking dye. b) Capture efficiency of cells/clusters in the PillarX device relative to a control of the spiked cells. c) Average cluster diameters of MDA-MB-231 and MDA-ECAD cells. d) PillarX capture profiles of the indicated cells/clusters in the different zones. Number of captured cells/clusters was quantified using the semi-automated ImageJ particles algorithm. Results are expressed as percent of captured cells/clusters per total cells spiked. e) Average cluster diameters in the PillarX device for the indicated cells. f) Distribution of clusters in the Pillar-device and the X-device for MDA-MB-231 and MDA-ECAD cells. g,h) E-cadherin (ECAD) relative intensities of MDA-MB-231 and MDA-ECAD clusters in the Pillar- and X-device. ECAD levels were measured by immuno-staining with an anti-ECAD antibody conjugated to Alexa Fluor 488 and normalized to a secondary antibody control. For (b,c,e,g,h) dots represent individual clusters. For (d,f) dots represent experimental repeats. Reported diameters were determined using the ImageJ Analyze Particles program. All data are mean \pm s.d. of at least 3 biological replicates. (b,c,g,h) *p*-values were calculated with an unpaired two-tailed Student's *t*-test. f) Data were analyzed by ordinary one-way ANOVA with Tukey's correction and 95% confidence intervals.

(Figure 6a–c). MCF10DCIS clusters were trapped in P1–P6 and in X1–X3, while MCF10DCIS-Mes clusters were found in P3–P6, and in X1–X8 (Figure 6d). The homogeneous distribution profile of MCF10DCIS-Mes cells/clusters in the X-device is consistent with a mixed epithelial phenotype (Figure 4c).

The analysis of cluster size in the device indicated that clusters with diameters $> 20 \mu\text{m}$ passed through the P6 gaps

and were distributed in the X-device (Figure 6e). The comparative analysis of cluster distribution of MCF10DCIS and MCF10DCIS-Mes, like in the case of MDA-MB-231 and MDA-ECAD clusters, depended on cluster size, cohesiveness, and epithelial cell identity. The majority (72%) of MCF10DCIS clusters were trapped between pillars, while less cohesive MCF10DCIS-Mes clusters were almost equally distributed between the

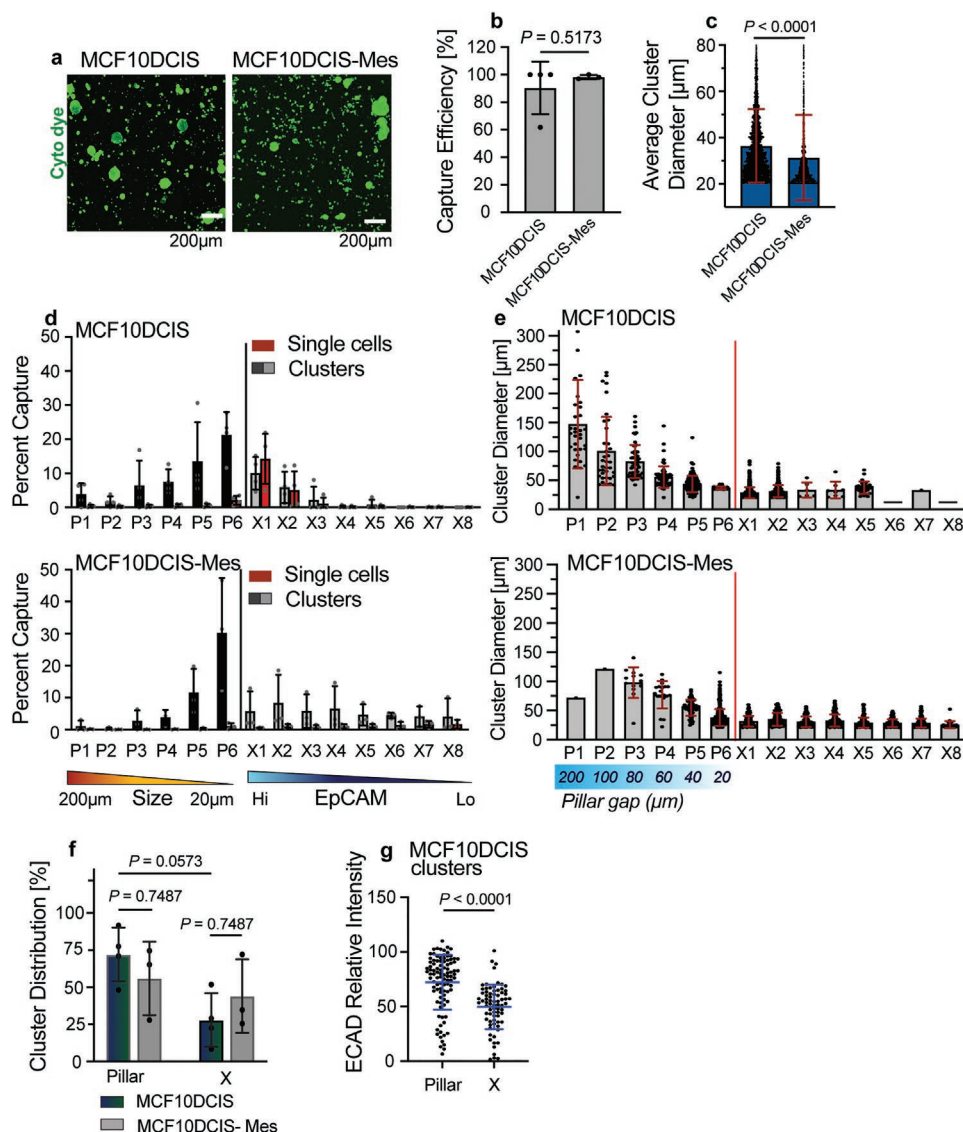


Figure 6. The PillarX device differentially sorts MCF10DCIS cells/clusters based on their mesenchymal state. MCF10DCIS and MCF10DCIS-Mes cells were cultured in low attachment conditions for 48 h, then mixed with 100 µL murine whole blood and anti-EpCAM MNPs, before loading into the PillarX device for profiling at 750 µL h⁻¹ (4000 cells/clusters per sample). a) Representative images of cells/clusters generated in low attachment culture conditions. Cells were labeled with a green live cell cytoplasmic (cyto) tracking dye. b) Capture efficiency of cells/clusters in the PillarX device relative to a control of the spiked cells. c) Average cluster diameters of MCF10DCIS and MCF10DCIS-Mes cells. d) PillarX capture profiles of the indicated cells/clusters in the different zones. Number of captured cells/clusters was quantified using the semi-automated ImageJ particles algorithm. Results expressed as percent of captured cells/clusters per total cells spiked. e) Average cluster diameters in the PillarX device for indicated cells. A dash indicates no clusters are present in that zone. f) Distribution of clusters in the Pillar- and the X-device for MCF10DCIS and MCF10DCIS-Mes cells. g) E-cadherin (ECAD) relative intensities of MCF10DCIS clusters in the Pillar- and X-device. ECAD levels were measured by immuno-staining with an anti-ECAD antibody conjugated to Alexa Fluor 488 and normalized to a secondary antibody control. For (b,c,e,g) dots represent individual clusters. For (d,f) dots represent experimental repeats. Reported diameters were determined using the ImageJ Analyze Particles program. All data are mean ± 3 s.d. of at least 3 biological replicates. (b,c,g) *p*-values were calculated with an unpaired two-tailed Student's *t*-test. f) Data were analyzed by ordinary one-way ANOVA with Tukey's correction and 95% confidence intervals.

Pillar- and the X-device (56% vs 44%, respectively, Figure 6f). On-chip immuno-staining revealed that MCF10DCIS X-device clusters had significantly lower E-cadherin levels compared with clusters trapped in the Pillar-device (Figure 6g), consistent with their reduced cohesiveness and increased ability to pass through the micro-pillars, and consistent with the results obtained by profiling MDA-MB-231 and MDA-ECAD clusters (Figure 5g,h).

Thus, the PillarX device efficiently captures and profiles cells and clusters, specifically based on their size, cohesiveness, and epithelial state. The more cohesive and larger breast cancer clusters have a greater likelihood of being trapped in the pillars, while the smaller and less-cohesive clusters pass through the pillars into the X-device, where they are captured according to their epithelial EpCAM expression levels.

1.6. The PillarX Device Sorts Clusters Based on Deformability

The ability to undergo shape changes provides cancer cells with an advantage in circulation.^[11] More deformable clusters can withstand shear forces exerted on their membrane and avoid rupture.^[2,11] The finding that less cohesive breast cancer clusters can change shape and move through narrow pillar gaps suggests that there is a correlation between cluster cohesiveness and deformability. This finding further suggests that the PillarX device can sort clusters according to differences in their biophysical properties.

To test these possibilities, we employed widefield time-lapse imaging and live cell tracking dyes to record the deformation events of clusters as they moved through pillars (Figure 7a,b).

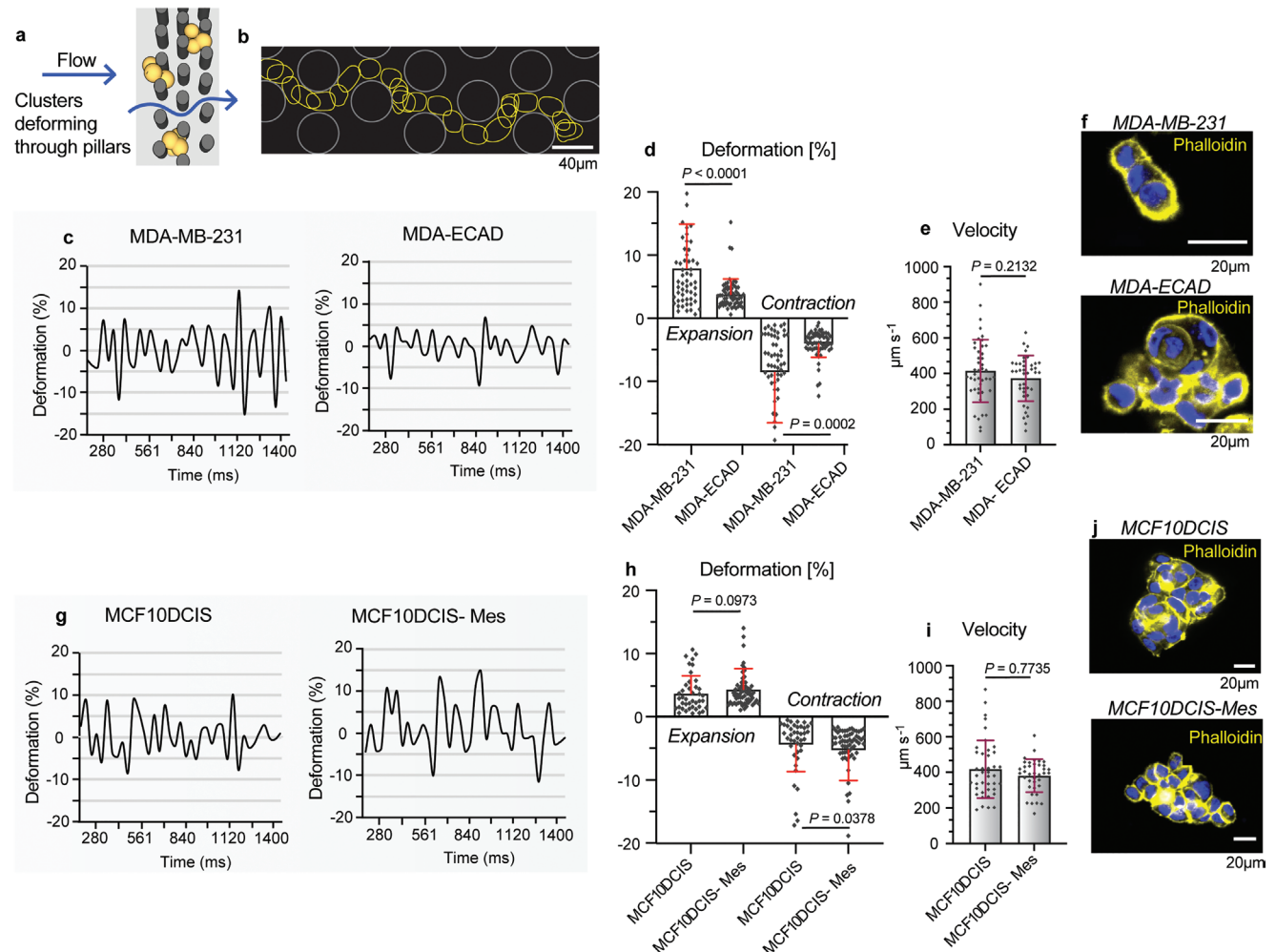


Figure 7. E-cadherin levels and mesenchymal states influence cluster deformability. a) Schematic of clusters moving through the pillars of the PillarX device. b) Representative video track of a cluster moving through P6 pillars. c) Representative positive and negative deformation events for a single MDA-MB-231 and single MDA-ECAD cluster moving through P6 of the PillarX device. d) Average area expansion and contraction deformation events for MDA-MB-231 and MDA-ECAD clusters moving through the pillars. e) Average velocities of MDA-MB-231 and MDA-ECAD clusters moving through pillars. f) Representative fluorescent images of MDA-MB-231 and MDA-ECAD clusters grown in low attachment conditions, highlighting differences in geometry. Cells were immuno-stained with Phalloidin-TRITC and DAPI. g) Representative positive and negative deformation events for a single MCF10DCIS and single MCF10DCIS-Mes cluster moving through P5 and P6 of the PillarX device. h) Average area expansion and contraction deformation events for MCF10DCIS and MCF10DCIS-Mes clusters moving through the pillars. i) Average velocities of indicated clusters moving through pillars. j) Representative fluorescent images of indicated clusters grown in low attachment conditions, highlighting differences in geometry. Cells were immuno-stained with Phalloidin-TRITC and DAPI. All Data are the mean ± s.d. of biological replicates (n = 3). p-values were calculated using an unpaired two-tailed Student's *t*-test. All dots represent individual clusters.

clusters from both cell lines moved at similar mean velocities through the pillars of $414 \mu\text{m s}^{-1}$ for MDA-MB-231 clusters and $372 \mu\text{m s}^{-1}$ for MDA-ECAD clusters. (Figure 7e; Figure S11a,b, Videos S1-S3, Supporting Information). Of note, the greater proportion of low-cohesive MDA-MB-231 clusters in the X-device relative to MDA-ECAD is likely the result of their ability to adopt a more elongated shape (Figure 7f).

Next, to investigate the correlation between cluster deformability and mesenchymal state, we monitored the extent of shape changes in MCF10DCIS and MCF10DCIS-Mes clusters as they traveled through the pillars. We found that the more mesenchymal MCF10DCIS-Mes clusters deformed to a greater extent than parental MCF10DCIS ($-5.3\% < d < 4.4\%$ for MCF10DCIS-Mes clusters and $-4.4\% < d < 3.7\%$ for MCF10DCIS clusters, Figure 7g,h). MCF10DCIS-Mes clusters had similar velocities as they move through the pillars relative to MCF10DCIS clusters (Figure 7i; Figure S11c,d and Videos S4–S7, Supporting Information). Finally, similar to MDA-MB-231 clusters, MCF10DCIS-Mes clusters displayed a more elongated, geometrical shapes that might increase their probability of passing through the pillars (Figure 7j). Higher cohesion, as seen in MCF10DCIS cells, results in a more rounded shape, and thus, a reduced fraction of deformable X-device clusters.

In addition, we examined the influence on cluster size on velocity and deformability by dividing the population of clusters into small (2-cell) and larger clusters (3–5 cells). Larger clusters had significantly greater areas than small clusters ($P = 0.0001$). We did not observe differences in velocities or deformation between the small- and large- populations considering MDA-MB-231 versus MDA-ECAD or MCF10DCIS versus MCF10DCIS-Mes clusters (Figure S12b–d,f,h, Supporting Information). Therefore, we observe that cluster size does not bias the velocity and deformability data when examining clusters composed by 2–5 cells flowing through P5 and P6.

Together, these results indicate that the increased deformability correlates with reduced cluster cohesion as seen with MDA-MB-231 relative to MDA-ECAD clusters, and MCF10DCIS-Mes relative to MCF10DCIS clusters. They further indicate that lower cluster cohesion is associated with the increased probability of clusters being trapped in X-part of the PillarX device, while cohesive clusters exhibit reduced deformation and become trapped between pillars. Hence, we show that the PillarX device efficiently measures cluster deformability and can be applied to sort clusters based on their biophysical properties.

To benchmark the PillarX performance, we compared the capture efficiencies to the X-device separately. The X-device is a demonstrated and published CTC-device,^[50,52] proven to capture CTCs with higher efficiency than CellSearch, the only FDA-approved CTC system. We found that the PillarX device captures breast cancer cells/ clusters as efficiently as the X-device run separately under the same conditions, and more cancer cells/ clusters than the Pillar-device run separately (Figure S13, Supporting Information). For example, for MCF10DCIS, PillarX capture efficiency is 90.4% (Figure 6b); which is very similar to the capture efficiency of the X-device (90.0%); however, PillarX outperforms the Pillar- device run alone (capture efficiency is 50.0%). Importantly, the serial combination of the Pillar- and X-device enables the ability to capture not only cells/

clusters according to epithelial state but also based on size and deformability.

1.7. The PillarX System Enables the Efficient Release of Viable Cells and Clusters

CTCs released from microfluidic devices have the potential to provide advanced information relating to drug-resistant populations and guide clinical treatments.^[76] We therefore developed a protocol for efficient release of cells/clusters from the PillarX device and subsequent culture conditions.

Captured cells/clusters were labeled with a green live cell tracking dye and NucBlue and released separately from the Pillar-device and the X-device by treatment with accutase, a mild proteolytic enzyme that weakens cell-adhesive interactions,^[77] followed by the application of a release flow rate ($5000 \mu\text{L h}^{-1}$). Following this protocol, MDA-MB-231 and MCF10DCIS cells were released with high efficiencies (93–99%, Figure S14a, Supporting Information). We assessed released cells for viability by flowing the cells off-chip and recording the percent of live cells (positive for green live cell tracking dye + NucBlue) relative to the total cells (NucBlue only). All cell lines showed a viability $> 70\%$, reflecting the gentle capture and release conditions (Figure S14b,c, Supporting Information). Released cells could also be transferred to cell culture media and kept in culture conditions to promote cell adhesion and growth. Notably, cultured MCF10DCIS cells released from the Pillar-device as compared to the X-device formed more colonies that display higher cell density, likely due to the higher concentration of clusters and increased cell–cell proximity, which favors proliferation (Figure S14d–g, Supporting Information). In comparison, cultures generated by released MDA-MB-231 cells were lower in density, mainly appearing as single dispersed cells, reflecting the lower level of cell–cell adhesiveness (Figure S14h, Supporting Information). Thus, the PillarX system enables the efficient release of viable cells and clusters that can be cultured, expanded, and further subjected to more detailed molecular analysis.

1.8. The PillarX Device Captures and Profiles CTCs and CTC Clusters from MDA-MB-231 Tumor-Bearing Mice and Breast Cancer Patients

Several studies have reported that CTC detection in various cancer patients is predictive of poor prognosis.^[3,10,13,78,79] Thus, we tested whether the PillarX device can capture individual CTCs and CTC clusters from the blood of tumor-bearing mice and patients with metastatic breast cancer, and we profiled them according to their biophysical properties.

Blood collected from immuno-compromised mice bearing MDA-MB-231 tumor xenografts and lung metastases (Figure S15, Supporting Information), was mixed with anti-EpCAM MNPs and analyzed with the PillarX device. CTC profiles revealed the presence of small, cohesive clusters that were captured in P6 of the Pillar-device and of more deformable smaller clusters captured in X4–X8 of the X-device (Figure 8a,b). Overall, from 8 mice analyzed, we captured between 10–244 single cells and 7–171 clusters per $500 \mu\text{L}$ of mouse blood,

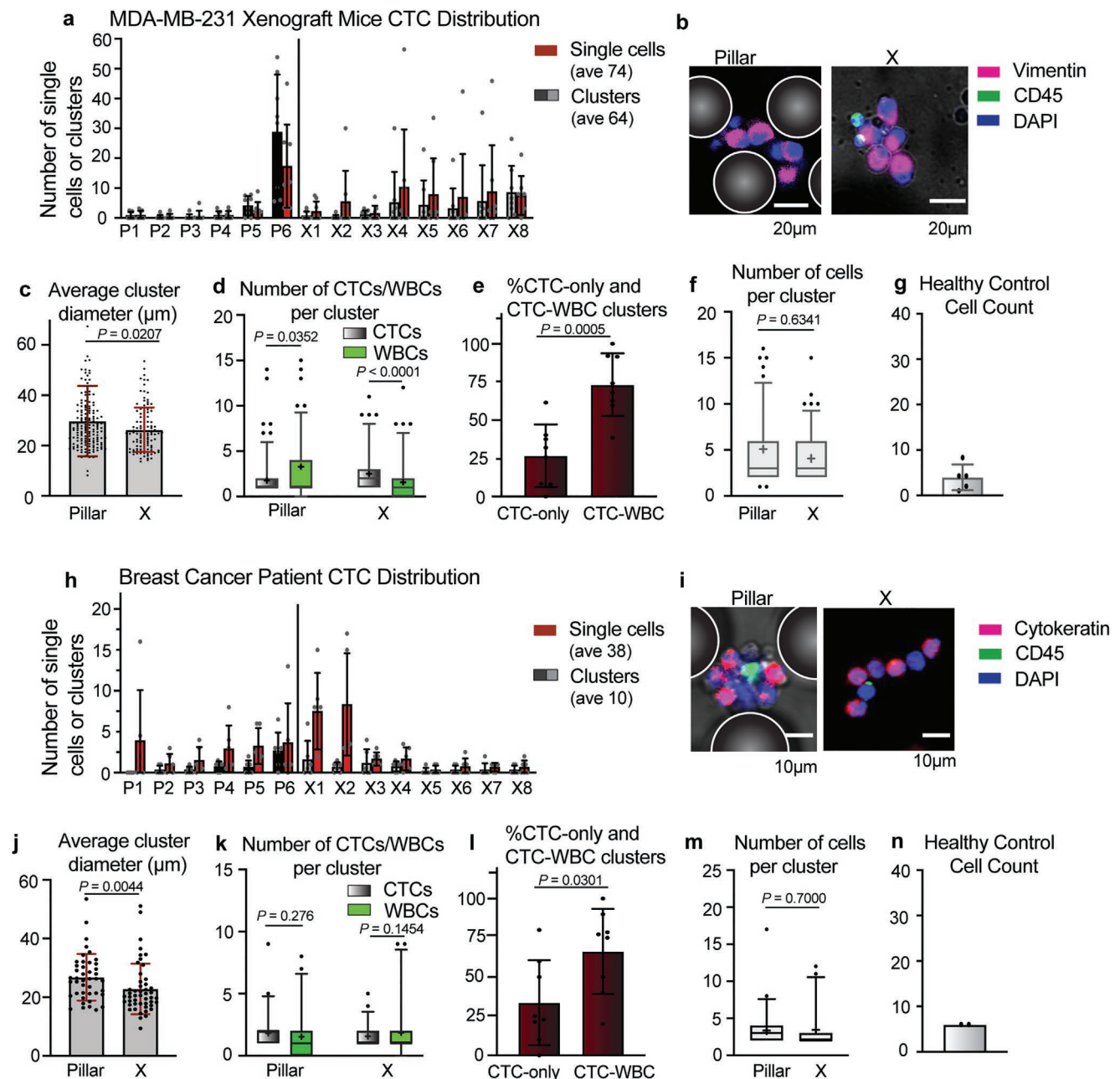


Figure 8. PillarX profiles of CTCs from mice bearing MDA-MB-231 tumor xenografts and from metastatic breast cancer patients. a) PillarX profile of MDA-MB-231 mouse CTCs. Blood samples (500 μL) collected by cardiac puncture from 8 mice were incubated with EpCAM-MNPs before loading in the PillarX device at 750 $\mu\text{L h}^{-1}$. Mean CTC counts per zone were determined by immuno-staining for vimentin⁺/DAPI⁺/CD45⁻ and applying a semi-automated counting method. Profile shows mean counts per zone. Average (ave) single CTCs and CTC clusters counts are shown in the key. b) Representative confocal microscopy images (63 \times) of MDA-MB-231 CTC clusters identified in the Pillar- and X-device by immuno-staining for vimentin⁺/DAPI⁺/CD45⁻. c) Average diameter of clusters in the Pillar- and X-device. d–f) The number of CTCs/WBCs per cluster, the percent CTC-only and CTC-WBC mixed clusters, and the average number of cells per cluster for the Pillar- and X-device, respectively. WBCs were identified as vimentin⁻/DAPI⁺/CD45⁺. g) False positive detection rate in the PillarX device. Number of vimentin⁺/DAPI⁺/CD45⁻ single cells detected in 500 μL of blood from healthy WT mice ($n = 5$). h) PillarX profiles of breast cancer patient CTCs. Blood samples (500 μL) were incubated with EpCAM-MNPs before loading in the PillarX device at 750 $\mu\text{L h}^{-1}$. Mean CTC counts are determined by immuno-staining as in (a) and quantification by applying a semi-automated counting method. Average (ave) CTC counts were obtained from 6 patients. i) Representative immuno-staining images of patient CTCs in the Pillar- and X-device obtained by confocal microscopy (63 \times). CTCs were identified as cytokeratin⁺/DAPI⁺/CD45⁻, based on the epithelial phenotype of breast cancer cells. j) Average diameter of clusters in the Pillar- and X-device. k, m) The number of CTCs/WBCs per cluster, the percent CTC-only and CTC-WBC clusters, and the average number of cells per cluster in the Pillar- and X-device, respectively. n) False positive rate per 500 μL of blood from healthy controls. Non-tumoral epithelial cells were identified as cytokeratin⁺/DAPI⁺/CD45⁻ from two healthy donors. MDA-MB-231 mouse data are mean \pm s.d. of biological replicates ($n = 8$). Human patient data are mean \pm s.d. of biological replicates ($n = 6$). Data plotted as box and whiskers display 5–95 percentile, with + indicating the mean. p -values were calculated with an unpaired two-tailed Student's t -test.

with a ratio of single CTCs versus clusters of 54% versus 46%, respectively (Table S3, Supporting Information). These data are consistent with previous reports of CTC counts from similar mouse models.^[39,80] In the X-device, single cells and clusters were trapped in the low-EpCAM zones (X4–X8), consistent with the mesenchymal nature of MDA-MB-231 CTCs.^[67] The X-clusters had an average diameter of 26 μm (Figure 8c), indicating that they can deform to pass through the 20 μm gap size in P6. The PillarX profile was remarkably similar to the in vitro profile generated by MDA-MB-231 clusters (Figure 5d), highlighting the capability of our device in profiling CTCs from animal models. MDA-MB-231 CTC clusters isolated from mice were frequently composed of heterogeneous mixtures of CTCs and WBCs, which accounted for 73% of total clusters (Figure 8e). The Pillar-device clusters were larger and had a greater percentage of WBCs relative to the X-device clusters (Figure 8c,d), indicating that WBCs contributed to cluster size. Additionally, CTC clusters from murine blood were generally small, ranging from an average of 5 and 4 cells per cluster in the Pillar- and X-device, respectively (Figure 8f), similar to previous reports.^[81] We also scored a false positive detection rate of 4 single cells/500 μL blood, which might represent non-cancerous mesenchymal cells present in the blood of healthy mice (Figure 8g).

To provide relevant translation perspective toward analysis of human CTCs, we profiled the peripheral blood of six patients with metastatic breast cancer. Of note, five out of these six patients were heavily pre-treated and had endocrine therapy-and/or chemotherapy-resistant disease (for clinical details and cancer histotype see Experimental Section and Table S4, Supporting Information). The analysis of the cluster distribution profiles in the PillarX device indicated the presence of small, cohesive clusters that were captured in the late zones of the Pillar-device, together with less cohesive and deformable clusters, which were captured in the early zones of the X-device (Figure 8h,i). Similar to data from our in vitro models, CTC clusters in the X-device had a smaller size compared to those of the Pillar-device (average diameters were 23 and 27 μm , respectively) (Figure 8j). About 66% of CTC clusters were composed of a mix of CTCs and WBCs (Figure 8k,l). The average cluster size from the Pillar- and X-device was 3-cells for both (Figure 8m), consistent with previously reported data.^[10] The range of CTCs found in patient blood was 12–79 single cells and 5–16 clusters (Table S4, Supporting Information), consistent with data from a previous study.^[30] We found 79% of CTCs were single cells and 21% were clusters. We detected a false-positive count of 6 cytokeratin-positive single cells per 500 μL of normal human blood (Figure 8n).

1.9. Profiling Primary Cells from a Murine Mammary Cancer Cell Line, and Relating to In Vivo Model

The amplification or overexpression of *HER2* in human mammary epithelial cells is sufficient to promote tumorigenic transformation by impacting on proliferation, survival, cell polarity, EMT, and invasiveness.^[82–84] We derived a murine mammary cancer cell line, MMCA, from a genetically engineered mouse model expressing the *HER2* oncogene and the pro-invasive endocytic *EPN3* gene in the mammary gland through the

MMTV-promoter,^[85] and profiled the cells in the PillarX device. These cells exhibited a partial EMT state, with high expression of *CDH1*, *CDH2*, *JUP*, *EPCAM*, *CLND3*, *CD44*, and *ITGB1*, and lower levels of *CDH11*, *TWIST1*, *ZEB1*, *VIM*, *SNAI1*, *SNAI2*, as confirmed with gene and protein expression (Figure S16a–d, Supporting Information). In adherent conditions, MMCA cells formed a dense monolayer (Figure S16e, Supporting Information), while under low attachment conditions, they formed compact clusters, with low aspect ratios, high circularity, solidity, and cell density (Figure S16f–k, Supporting Information). Clusters and cells grown under low attachment conditions were captured in the PillarX device with high efficiency (Figure S17a–c, Supporting Information). The PillarX profiles revealed that the clusters were primarily captured in the Pillar-device relative to the X-device (76% vs 24%) and were trapped in the high-EpCAM zones of the X-device, consistent with their epithelial phenotype (Figure S17d–f, Supporting Information).

Finally, we compared the primary cell line profiles with CTCs captured from a MMTV-Neu mouse model. These mice developed breast tumors between \approx 8–9 months of age, after which they were sacrificed and the blood was analyzed in our device. We found mainly large CTC-WBC clusters that were primarily (88% of clusters) trapped in the Pillar-device (Figure S18 and Table S5, Supporting Information). The majority of MMTV-Neu mouse clusters were captured between pillars, consistent with the in vitro MMCA data (Figure S18a, Supporting Information). The less-deformable properties of the in vivo clusters could highlight the importance of maintaining cell cohesiveness in the circulation of invasive cancer mouse models.

Together, this validation of the PillarX device for mouse and human breast cancer CTC profiling represents a proof of principle that could be applied toward tumor diagnosis and treatment monitoring or tailoring.

1.10. Outlook

CTCs and CTC clusters play important roles in the metastatic seeding of carcinomas and are clinically associated with poor prognosis.^[86] Here, we described the development of a microfluidic device that profiles CTCs and CTC clusters based on their physical properties and on the expression of an epithelial marker. Through genetic manipulation of E-cadherin and selection of partial EMT phenotypes, we showed that cohesive and less deformable clusters are preferentially captured in the Pillar-device relative to the X-device. In particular, E-cadherin expression in MDA-MB-231 resulted in increased cluster cohesion and the majority of clusters trapping between pillars; while mesenchymal transformation of MCF10DCIS clusters shifted the profile toward X-device capture and corresponded with increased deformability.

Different methods exist to measure mechanical properties of cells, including indentation/ compression and magnetic twisting cytometry for adhered cells and micro-aspiration techniques, stretching with optical tweezers, and cell rheometry microfluidics for suspended cells.^[87–89] These systems have been extensively applied toward single cells but are not well characterized for clusters. Thus, here we present a system that can provide a readout of relative cluster mechanical properties inside a single device while keeping clusters intact.

Cluster deformability can be influenced by many factors, including intrinsic differences in the physical rigidity of individual cells, alterations in cell–cell interactions or increased ability of cells to rearrange their position with respect to its neighbors.^[38,90] In our system, we provided direct evidence that altering cell cohesion influences the shape-changing ability of the clusters, as observed by their constriction through pillar gaps or their rearrangement into elongated geometries. The ability of our device to sort breast cancer clusters based on these physical properties (cohesion, deformability, rigidity, and shape) represents an important advance in microfluidic cell profiling; which, in the future, may be instrumental to establish an unequivocal link between deformability and metastatic propensity.

We also found that the presence of frequent heterotypic CTC-WBC clusters in blood samples from tumor-bearing mice and breast cancer patients. CTC-WBC clusters were found in both the Pillar- and X-device; the WBC contribution in the in vivo models ranged from 61–77% in the Pillar-device and 58–72% in the X-device. It has been reported that the association of cancer cells with WBCs can allow clusters to escape immune surveillance, provides survival advantages in circulation and increases metastatic seeding.^[39,81] Furthermore, CTC-WBC clusters may have increased mechanical protection against shear stress in the bloodstream.^[91]

Overall, our microfluidic PillarX device provides a system that can be applied to the study of in vivo mouse cancer models and patients to deepen our understanding of the metastatic process and response to treatments. In the future, a device for profiling CTC clusters based on defined biophysical features could be applied toward clinical applications as a diagnostic/prognostic tool and to help guide treatment decision making.

Supporting Information

Supporting Information is available from the Wiley Online Library or from the author.

Acknowledgements

The work is supported by grants from the following agencies: AIRC – Fondazione AIRC per la ricerca sul cancro [Fellowship iCARE-2 2018 (Ref. 22 433) to B.G., AIRC fellowship “Isabella Gallo” (Ref. 22 386) to G.G.] and grants AIRC IG 18 621 and 5XMillie 22 759 to G.S., AIRC IG 24 415 and Worldwide Cancer Research (20-0094) to S.S., AIRC IG 23 060 to P.P.D.F.; the Italian Ministry of University and Scientific Research (MIUR) (PRIN 2017, Prot. 2017HWTP2K to G.S., PRIN 2017, Prot. 2017E5L5P3 to S.S.; Prot. 2015XS92CC to P.P.D.F.). This work was also partially supported by the Italian Ministry of Health with Ricerca Corrente to P.P.D.F. Mouse study approval. All animal studies were conducted with the approval of Italian Minister of Health (27/2015-PR) and were performed in accordance with the Italian law (D.lgs.26/2014), which enforces Dir. 2010/63/EU (Directive 2010/63/EU of the European Parliament and of the Council on the protection of animals used for scientific purposes). Human Patients: Breast cancer patients included in this study were enrolled in the ongoing OPTIMAL trial (ClinicalTrials.gov: NCT04001725; EudraCT (2019-000105-73), which is evaluating the impact of adding metformin to glucocorticoids in patients with brain metastases from melanoma, breast or lung cancer. Enrolled patients consented to donate their blood samples for research purposes. The

study was approved by the Ethics Committee of Fondazione IRCCS Istituto Nazionale dei Tumori (Milan, Italy).

Conflict of Interest

The authors declare no conflict of interest.

Author Contributions

B.G. and G.S. conceived and designed the experiments; B.G., M.M., B.H., A.F. and G.G. performed the experiments, simulations, and analyzed the data; E.M., S.M., D.P., and P.M. designed imaging analytical tools; Z.W. and Q.L. designed the microfluidic devices; F.P. performed immunohistochemistry experiments and analysis; B.H., A.F., S.S., E.F., and K.H. created the mouse models and performed blood and tumor isolation; G.V.B. performed transmission electron microscopy; C.V. and R.L. managed the breast cancer patient samples; S.M. and A.D. performed western blotting, and bacterial amplification experiments; B.G., M.L., P.P.D.F., R.G., S.O.K., and G.S. designed the research, analyzed and interpreted the data, and wrote the paper. Each author contributed to writing the paper.

Data Availability Statement

The data that support the findings of this study are available from the corresponding author upon reasonable request.

Keywords

breast cancer, deformability, diagnostics, microfluidics, nanoparticles

Received: October 7, 2021

Revised: March 7, 2022

Published online: March 28, 2022

- [1] C. Alix-Panabieres, K. Pantel, *Clin. Chem.* **2013**, *59*, 110.
- [2] V. Gensbittel, M. Krater, S. Harlepp, I. Busnelli, J. Guck, J. G. Goetz, *Dev. Cell* **2021**, *56*, 164.
- [3] N. Aceto, A. Bardia, D. T. Miyamoto, M. C. Donaldson, B. S. Wittner, J. A. Spencer, M. Yu, A. Pely, A. Engstrom, H. Zhu, B. W. Brannigan, R. Kapur, S. L. Stott, T. Shioda, S. Ramaswamy, D. T. Ting, C. P. Lin, M. Toner, D. A. Haber, S. Maheswaran, *Cell* **2014**, *158*, 1110.
- [4] S. Amintas, A. Bedel, F. Moreau-Gaudry, J. Boutin, L. Buscail, J. P. Merlio, V. Vendrely, S. Dabernat, E. Buscail, *Int. J. Mol. Sci.* **2020**, *21*, 7.
- [5] K. J. Cheung, V. Padmanaban, V. Silvestri, K. Schipper, J. D. Cohen, A. N. Fairchild, M. A. Gorin, J. E. Verdone, K. J. Pienta, J. S. Bader, A. J. Ewald, *Proc. Natl. Acad. Sci. U. S. A.* **2016**, *113*, E854.
- [6] S. L. Stott, C. H. Hsu, D. I. Tsukrov, M. Yu, D. T. Miyamoto, B. A. Waltman, S. M. Rothenberg, A. M. Shah, M. E. Smas, G. K. Korir, F. P. Floyd, Jr., A. J. Gilman, J. B. Lord, D. Winokur, S. Springer, D. Irimia, S. Nagrath, L. V. Sequist, R. J. Lee, K. J. Isselbacher, S. Maheswaran, D. A. Haber, M. Toner, *Proc. Natl. Acad. Sci. U. S. A.* **2010**, *107*, 18392.
- [7] M. Yu, A. Bardia, B. S. Wittner, S. L. Stott, M. E. Smas, D. T. Ting, S. J. Isakoff, J. C. Ciciliano, M. N. Wells, A. M. Shah, K. F. Concannon, M. C. Donaldson, L. V. Sequist, E. Brachtel, D. Sgroi, J. Baselga, S. Ramaswamy, M. Toner, D. A. Haber, S. Maheswaran, *Science* **2013**, *339*, 580.

- [8] I. Krol, F. D. Schwab, R. Carbone, M. Ritter, S. Picocchi, M. L. De Marni, G. Stepien, G. M. Franchi, A. Zanardi, M. D. Rissoglio, A. Covelli, G. Guidi, D. Scarinci, F. Castro-Giner, L. Mazzarella, C. Doglioni, F. Borghi, P. Milani, C. Kurzeder, W. P. Weber, N. Aceto, *Br. J. Cancer* **2021**, 125, 23.
- [9] A. M. Larsson, S. Jansson, P. O. Bendahl, C. Levin Tykjaer Jorgensen, N. Loman, C. Graffman, L. Lundgren, K. Aaltonen, L. Ryden, *Breast Cancer Res.* **2018**, 20, 48.
- [10] C. Costa, L. Muineloro-Romay, V. Cebeby-Lopez, T. Pereira-Veiga, I. Martinez-Pena, M. Abreu, A. Abalo, R. M. Lago-Leston, C. Abuin, P. Palacios, J. Cueva, R. Pineiro, R. Lopez-Lopez, *Cancers (Basel)* **2020**, 12, 5.
- [11] Y. Xin, X. Chen, X. Tang, K. Li, M. Yang, W. C. Tai, Y. Liu, Y. Tan, *Biophys. J.* **2019**, 116, 1803.
- [12] K. J. Cheung, E. Gabrielson, Z. Werb, A. J. Ewald, *Cell* **2013**, 155, 1639.
- [13] Z. Diamantopoulou, F. Castro-Giner, N. Aceto, *J. Exp. Med.* **2020**, 217,
- [14] H. Son, A. Moon, *Toxicol. Res.* **2010**, 26, 245.
- [15] M. E. Francart, J. Lambert, A. M. Vanwynsberghe, E. W. Thompson, M. Bourcy, M. Polette, C. Gilles, *Dev. Dyn.* **2018**, 247, 432.
- [16] W. Xu, R. Mezenцев, B. Kim, L. Wang, J. McDonald, T. Sulchek, *PLoS One* **2012**, 7, e46609.
- [17] H. Byun, T. R. Hillman, J. M. Higgins, M. Diez-Silva, Z. Peng, M. Dao, R. R. Dasari, S. Suresh, Y. Park, *Acta Biomater.* **2012**, 8, 4130.
- [18] E. M. Darling, S. Zauscher, J. A. Block, F. Guilak, *Biophys. J.* **2007**, 92, 1784.
- [19] Z. Liu, S. J. Lee, S. Park, K. Konstantopoulos, K. Glunde, Y. Chen, I. Barman, *FASEB J.* **2020**, 34, 9307.
- [20] Q. S. Li, G. Y. Lee, C. N. Ong, C. T. Lim, *Biochem. Biophys. Res. Commun.* **2008**, 374, 609.
- [21] F. Broders-Bondon, T. H. Nguyen Ho-Boulidoires, M. E. Fernandez-Sanchez, E. Farge, *J. Cell Biol.* **2018**, 217, 1571.
- [22] L. Chin, Y. Xia, D. E. Discher, P. A. Janmey, *Curr. Opin. Chem. Eng.* **2016**, 11, 77.
- [23] B. D. Hoffman, J. C. Crocker, *Annu. Rev. Biomed. Eng.* **2009**, 11, 259.
- [24] L. D. Osborne, G. Z. Li, T. How, E. T. O'Brien, G. C. Blobe, R. Superfine, K. Myhre, *Mol. Biol. Cell* **2014**, 25, 3528.
- [25] H. T. Tse, D. R. Gossett, Y. S. Moon, M. Masaeli, M. Sohsman, Y. Ying, K. Mislack, R. P. Adams, J. Rao, D. Di Carlo, *Sci. Transl. Med.* **2013**, 5, 212ra163.
- [26] S. E. Cross, Y. S. Jin, J. Tondre, R. Wong, J. Rao, J. K. Gimzewski, *Nanotechnology* **2008**, 19, 384003.
- [27] M. Labib, S. O. Kelley, *Mol. Oncol.* **2021**, 15, 1622.
- [28] K. Yap, E. N. Cohen, J. M. Reuben, J. D. Khoury, *Curr. Hematol. Malig. Rep.* **2019**, 14, 353.
- [29] Y. Zeng, T. Wang, *Anal. Bioanal. Chem.* **2013**, 405, 5743.
- [30] S. Nagrath, L. V. Sequist, S. Maheswaran, D. W. Bell, D. Irimia, L. Ulkus, M. R. Smith, E. L. Kwak, S. Digumarthy, A. Muzikansky, P. Ryan, U. J. Balis, R. G. Tompkins, D. A. Haber, M. Toner, *Nature* **2007**, 450, 1235.
- [31] M. A. Witek, R. D. Aufforth, H. Wang, J. W. Kamande, J. M. Jackson, S. R. Pullagurla, M. L. Hupert, J. Usary, W. Z. Wysham, D. Hilliard, S. Montgomery, V. Bae-Jump, L. A. Carey, P. A. Gehrig, M. I. Milowsky, C. M. Perou, J. T. Soper, Y. E. Whang, J. J. Yeh, G. Martin, S. A. Soper, *NPJ Precis Oncol* **2017**, 1, 24.
- [32] J. P. Gleghorn, E. D. Pratt, D. Denning, H. Liu, N. H. Bander, S. T. Tagawa, D. M. Nanus, P. A. Giannakakou, B. J. Kirby, *Lab Chip* **2010**, 10, 27.
- [33] W. Zhao, C. H. Cui, S. Bose, D. Guo, C. Shen, W. P. Wong, K. Halvorsen, O. C. Farokhzad, G. S. Teo, J. A. Phillips, D. M. Dorfman, R. Karnik, J. M. Karp, *Proc. Natl. Acad. Sci. U. S. A.* **2012**, 109, 19626.
- [34] E. Ozkumur, A. M. Shah, J. C. Ciciliano, B. L. Emmink, D. T. Miyamoto, E. Brachtel, M. Yu, P. I. Chen, B. Morgan, J. Trautwein, A. Kimura, S. Sengupta, S. L. Stott, N. M. Karabacak, T. A. Barber, J. R. Walsh, K. Smith, P. S. Spuhler, J. P. Sullivan, R. J. Lee, D. T. Ting, X. Luo, A. T. Shaw, A. Bardia, L. V. Sequist, D. N. Louis, S. Maheswaran, R. Kapur, D. A. Haber, M. Toner, *Sci. Transl. Med.* **2013**, 5, 179ra47.
- [35] H. Kim, M. Lim, J. Y. Kim, S. J. Shin, Y. K. Cho, C. H. Cho, *Diagnostics (Basel)* **2020**, 10,
- [36] G. Vona, A. Sabile, M. Louha, V. Sitruk, S. Romana, K. Schutze, F. Capron, D. Franco, M. Pazzagli, M. Vekemans, B. Lacour, C. Brechot, P. Paterlini-Brechot, *Am. J. Pathol.* **2000**, 156, 57.
- [37] Y. Hong, F. Fang, Q. Zhang, *Int. J. Oncol.* **2016**, 49, 2206.
- [38] S. H. Au, B. D. Storey, J. C. Moore, Q. Tang, Y. L. Chen, S. Javaid, A. F. Sarioglu, R. Sullivan, M. W. Madden, R. O'Keefe, D. A. Haber, S. Maheswaran, D. M. Langenau, S. L. Stott, M. Toner, *Proc. Natl. Acad. Sci. U. S. A.* **2016**, 113, 4947.
- [39] B. M. Szczerba, F. Castro-Giner, M. Vetter, I. Krol, S. Gkoutela, J. Landin, M. C. Scheidmann, C. Donato, R. Scherrer, J. Singer, C. Beisel, C. Kurzeder, V. Heinzelmann-Schwarz, C. Rochlitz, W. P. Weber, N. Beerenwinkel, N. Aceto, *Nature* **2019**, 566, 553.
- [40] M. Zeinali, M. Lee, A. Nadhan, A. Mathur, C. Hedman, E. Lin, R. Harouaka, M. S. Wicha, L. Zhao, N. Palanisamy, M. Hafner, R. Reddy, G. P. Kalemkerian, B. J. Schneider, K. A. Hassan, N. Ramnath, S. Nagrath, *Cancers (Basel)* **2020**, 12, 127.
- [41] A. Kulasinghe, J. Zhou, L. Kenny, I. Papautsky, C. Punyadeera, *Cancers (Basel)* **2019**, 11, 89.
- [42] S. H. Au, J. Edd, A. E. Stoddard, K. H. K. Wong, F. Fachin, S. Maheswaran, D. A. Haber, S. L. Stott, R. Kapur, M. Toner, *Sci. Rep.* **2017**, 7, 2433.
- [43] J. Che, V. Yu, E. B. Garon, J. W. Goldman, D. Di Carlo, *Lab Chip* **2017**, 17, 1452.
- [44] M. Aghaamoo, Z. Zhang, X. Chen, J. Xu, *Biomicrofluidics* **2015**, 9, 034106.
- [45] S. J. Hymel, H. Fujioka, D. B. Khismatullin, *bioRxiv* **2021**.
- [46] W. Zhang, K. Kai, D. S. Choi, T. Iwamoto, Y. H. Nguyen, H. Wong, M. D. Landis, N. T. Ueno, J. Chang, L. Qin, *Proc. Natl. Acad. Sci. U. S. A.* **2012**, 109, 18707.
- [47] M. Urbanska, H. E. Munoz, J. Shaw Bagnall, O. Otto, S. R. Manalis, D. Di Carlo, J. Guck, *Nat. Methods* **2020**, 17, 587.
- [48] R. Riahi, P. Gogoi, S. Sepehri, Y. Zhou, K. Handique, J. Godsey, Y. Wang, *Int. J. Oncol.* **2014**, 44, 1870.
- [49] M. K. F. Hakim, I. Alemzadeh, M. Vossoughi, *Anal. Chim. Acta* **2021**, 1186, 339115.
- [50] R. M. Mohamadi, J. D. Besant, A. Mephram, B. Green, L. Mahmoudian, T. Gibbs, I. Ivanov, A. Malvea, J. Stojcic, A. L. Allan, L. E. Lowes, E. H. Sargent, R. K. Nam, S. O. Kelley, *Angew. Chem., Int. Ed.* **2015**, 54, 139.
- [51] J. D. Besant, R. M. Mohamadi, P. M. Aldridge, Y. Li, E. H. Sargent, S. O. Kelley, *Nanoscale* **2015**, 7, 6278.
- [52] B. J. Green, V. Nguyen, E. Atenafu, P. Weeber, B. T. V. Duong, P. Thiagalingam, M. Labib, R. M. Mohamadi, A. R. Hansen, A. M. Joshua, S. O. Kelley, *Anal. Chem.* **2019**, 91, 9348.
- [53] C. Alix-Panabieres, K. Pantel, *Nat. Rev. Cancer* **2014**, 14, 623.
- [54] L. Keller, S. Werner, K. Pantel, *Cell Stress* **2019**, 3, 165.
- [55] Y. Dong, A. M. Skelley, K. D. Merdek, K. M. Sprott, C. Jiang, W. E. Pierceall, J. Lin, M. Stocum, W. P. Carney, D. A. Smirnov, *J. Mol. Diagn.* **2013**, 15, 149.
- [56] B. J. Green, L. Kermanshah, M. Labib, S. U. Ahmed, P. N. Silva, L. Mahmoudian, I. H. Chang, R. M. Mohamadi, J. V. Rocheleau, S. O. Kelley, *ACS Appl. Mater. Interfaces* **2017**, 9, 20435.
- [57] A. Marrella, A. Fedi, G. Varani, I. Vaccari, M. Fato, G. Firpo, P. Guida, N. Aceto, S. Scaglione, *PLoS One* **2021**, 16, e0245536.
- [58] S. C. Hur, N. K. Henderson-MacLennan, E. R. McCabe, D. Di Carlo, *Lab Chip* **2011**, 11, 912.

- [59] O. Otto, P. Rosendahl, A. Mietke, S. Golfer, C. Herold, D. Klaue, S. Girardo, S. Pagliara, A. Ekpenyong, A. Jacobi, M. Wobus, N. Topfner, U. F. Keyser, J. Mansfeld, E. Fischer-Friedrich, J. Guck, *Nat. Methods* **2015**, *12*, 199.
- [60] S. Byun, S. Son, D. Amodei, N. Cermak, J. Shaw, J. H. Kang, V. C. Hecht, M. M. Winslow, T. Jacks, P. Mallick, S. R. Manalis, *Proc. Natl. Acad. Sci. U. S. A.* **2013**, *110*, 7580.
- [61] N. Aceto, M. Toner, S. Maheswaran, D. A. Haber, *Trends Cancer* **2015**, *1*, 44.
- [62] V. L. Chin, C. L. Lim, *Stem Cell Investig.* **2019**, *6*, 25.
- [63] L. Ombrato, I. Malanchi, *Crit. Rev. Oncog.* **2014**, *19*, 349.
- [64] H. C. Bruner, P. W. B. Derksen, *Cold Spring Harbor Perspect. Biol.* **2018**, *10*, a029330.
- [65] X. Lin, X. Shang, G. Manorek, S. B. Howell, *PLoS One* **2013**, *8*, e67496.
- [66] R. David, O. Luu, E. W. Damm, J. W. Wen, M. Nagel, R. Winklbauer, *Development* **2014**, *141*, 3672.
- [67] R. Cailleau, M. Olive, Q. V. Cruciger, *In Vitro* **1978**, *14*, 911.
- [68] K. J. Chavez, S. V. Garimella, S. Lipkowitz, *Breast Dis.* **2010**, *32*, 35.
- [69] A. Labernadie, T. Kato, A. Bragues, X. Serra-Picamal, S. Derzsi, E. Arwert, A. Weston, V. Gonzalez-Tarrago, A. Elosegui-Artola, L. Albertazzi, J. Alcaraz, P. Roca-Cusachs, E. Sahai, X. Trepas, *Nat. Cell Biol.* **2017**, *19*, 224.
- [70] T. Y. Na, L. Schecterson, A. M. Mendonsa, B. M. Gumbiner, *Proc. Natl. Acad. Sci. U. S. A.* **2020**, *117*, 5931.
- [71] V. Padmanaban, I. Krol, Y. Suhail, B. M. Szczerba, N. Aceto, J. S. Bader, A. J. Ewald, *Nature* **2019**, *573*, 439.
- [72] G. C. Russo, M. N. Karl, D. Clark, J. Cui, R. Carney, B. Su, B. Starich, T.-S. Lih, Q. Zhang, P.-H. Wu, M.-H. Lee, H. S. Leong, H. Zhang, D. Wirtz, *bioRxiv* **2020**.
- [73] F. R. Miller, S. J. Santner, L. Tait, P. J. Dawson, *J. Natl. Cancer Inst.* **2000**, *92*, 1185a.
- [74] J. Yang, P. Antin, G. Bex, C. Blanpain, T. Brabletz, M. Bronner, K. Campbell, A. Cano, J. Casanova, G. Christofori, S. Dedhar, R. Derynck, H. L. Ford, J. Fuxe, A. Garcia de Herreros, G. J. Goodall, A. K. Hadjantonakis, R. J. Y. Huang, C. Kalcheim, R. Kalluri, Y. Kang, Y. Khew-Goodall, H. Levine, J. Liu, G. D. Longmore, S. A. Mani, J. Massague, R. Mayor, D. McClay, K. E. Mostov, et al., *Nat. Rev. Mol. Cell Biol.* **2020**, *21*, 341.
- [75] M. Hu, J. Yao, D. K. Carroll, S. Weremowicz, H. Chen, D. Carrasco, A. Richardson, S. Violette, T. Nikolskaya, Y. Nikolsky, E. L. Bauerlein, W. C. Hahn, R. S. Gelman, C. Allred, M. J. Bissell, S. Schnitt, K. Polyak, *Cancer Cell* **2008**, *13*, 394.
- [76] S. Maheswaran, D. A. Haber, *Cancer Res.* **2015**, *75*, 2411.
- [77] D. Salzig, A. Schmiermund, P. P. Grace, C. Elseberg, C. Weber, P. Czermak, *Open Biomed. Eng. J.* **2013**, *7*, 147.
- [78] C. Wang, Z. Mu, I. Chervoneva, L. Austin, Z. Ye, G. Rossi, J. P. Palazzo, C. Sun, M. Abu-Khalaf, R. E. Myers, Z. Zhu, Y. Ba, B. Li, L. Hou, M. Cristofanilli, H. Yang, *Breast Cancer Res. Treat.* **2017**, *161*, 83.
- [79] M. Iwatsuki, K. Toyoshima, M. Watanabe, N. Hayashi, T. Ishimoto, K. Eto, S. Iwagami, Y. Baba, N. Yoshida, A. Hayashi, Y. Ohta, H. Baba, *Br. J. Cancer* **2013**, *109*, 2829.
- [80] L. Cleris, M. G. Daidone, E. Fina, V. Cappelletti, *Cells* **2019**, *8*, 683.
- [81] M. Saini, B. M. Szczerba, N. Aceto, *Cancer Res.* **2019**, *79*, 6067.
- [82] D. Yu, J. Hamada, H. Zhang, G. L. Nicolson, M. C. Hung, *Oncogene* **1992**, *7*, 2263.
- [83] S. Ingthorsson, K. Andersen, B. Hilmarsson, G. M. Maelandsmo, M. K. Magnusson, T. Gudjonsson, *Oncogene* **2016**, *35*, 4244.
- [84] M. M. Moasser, *Oncogene* **2007**, *26*, 6469.
- [85] I. Schiano Lomoriello, G. Giangreco, C. Iavarone, C. Tordonato, G. Caldieri, G. Serio, S. Confalonieri, S. Freddi, F. Bianchi, S. Pirroni, G. Bertalot, G. Viale, D. Disalvatore, D. Tosoni, M. G. Malabarba, A. Disanza, G. Scita, S. Pece, B. K. Pilcher, M. Vecchi, S. Sigismund, P. P. Di Fiore, *Nat. Commun.* **2020**, *11*, 3020.
- [86] M. Giuliano, A. Shaikh, H. C. Lo, G. Arpino, S. De Placido, X. H. Zhang, M. Cristofanilli, R. Schiff, M. V. Trivedi, *Cancer Res.* **2018**, *78*, 845.
- [87] C. T. Lim, E. H. Zhou, S. T. Quek, *J. Biomech.* **2006**, *39*, 195.
- [88] P. Pereira, M. P. Valignat, J. Bico, O. Theodoly, *Biomicrofluidics* **2013**, *7*, 024111.
- [89] J. Guck, R. Ananthakrishnan, H. Mahmood, T. J. Moon, C. C. Cunningham, J. Kas, *Biophys. J.* **2001**, *81*, 767.
- [90] E. D. Wrenn, A. Yamamoto, B. M. Moore, Y. Huang, M. McBirney, A. J. Thomas, E. Greenwood, Y. F. Rabena, H. Rahbar, S. C. Partridge, K. J. Cheung, *Cell* **2020**, *183*, 395.
- [91] J. Shaw Bagnall, S. Byun, S. Begum, D. T. Miyamoto, V. C. Hecht, S. Maheswaran, S. L. Stott, M. Toner, R. O. Hynes, S. R. Manalis, *Sci. Rep.* **2015**, *5*, 18542.